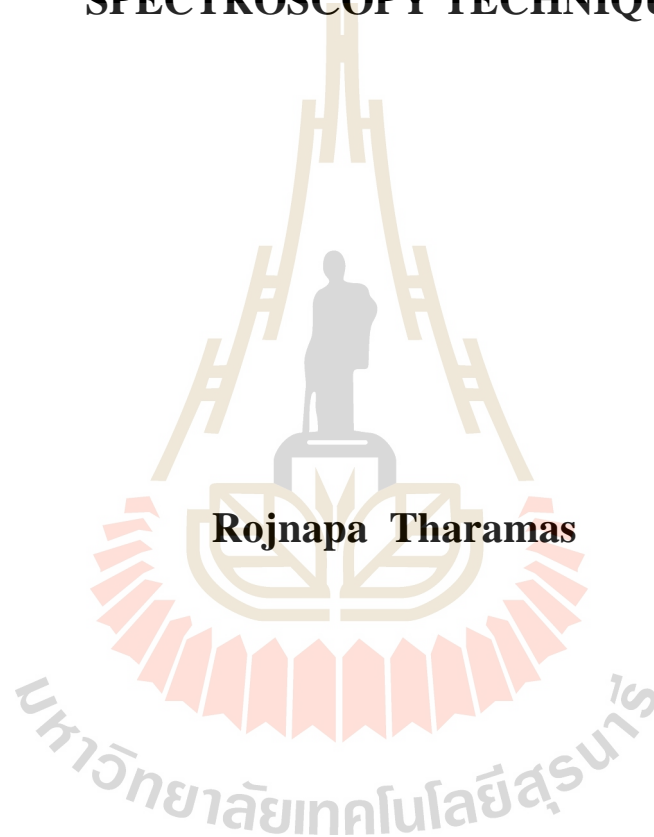# EFFECTS OF TEMPERATURE AND ELECTRIC FIELD

ON LOCAL STRUCTURE OF Pb(Zr,Ti)O$_3$ SINGLE

CRYSTALS STUDIED BY X-RAY ABSORPTION

SPECTROSCOPY TECHNIQUE

Rojnapa Tharamas

A Thesis Submitted in Partial Fulfillment of the Requirements for the

Degree of Master of Science in Applied Physics

Suranaree University of Technology

Academic Year 2016

การศึกษาผลของอุณหภูมิและสนามไฟฟ้าต่อโครงสร้างเฉพาะบริเวณของผลึกเดี่ยว Pb(Zr,Ti)O$_3$ โดยเทคนิคสเปกโทรสโกปีการดูดกลืนรังสีเอ็กซ์

นางสาวโรจน์นภา ธารามาศ

EFFECTS OF TEMPERATURE AND ELECTRIC FIELD ON LOCAL STRUCTURE OF Pb(Zr,Ti)O$_3$ SINGLE CRYSTALS STUDIED BY X-RAY ABSORPTION SPECTROSCOPY TECHNIQUE

Suranaree University of Technology has approved this thesis submitted in partial fulfillment of the requirements for Master's Degree.

Thesis Examining Committee

_____

(Asst. Prof. Dr. Worawat Meevasana)

Chairperson

_____

(Assoc. Prof. Dr. Rattikorn Yimnirun)

Member (Thesis Advisor)

_____

(Dr. Saroj Rujirawat)

Member

_____

(Assoc. Prof. Dr. Prayoon Songsiriritthigul)

Member

_____

(Dr. Pinit Kidkhunthod)

Member

_____   _____

(Prof. Dr. Santi Maensiri)   (Prof. Dr. Santi Maensiri)

Acting Vice Rector for Academic   Dean of Institute of Science

Affairs and Internationalization

โรจน์นภา ธารามาศ : ผลของอุณหภูมิและสนามไฟฟ้าต่อโครงสร้างเฉพาะบริเวณของ
ผลึกเดี่ยว Pb(Zr,Ti)O$_3$ ศึกษาโดยเทคนิคสเปกโทรสโกปีการดูดกลืนรังสีเอ็กซ์.
อาจารย์ที่ปรึกษา : รองศาสตราจารย์ ดร.รัตติกร ยิ้มนิรัญ, 86 หน้า.

วิทยานิพนธ์นี้มุ่งศึกษาผลของอุณหภูมิและสนามไฟฟ้าต่อโครงสร้างเฉพาะบริเวณของ
ผลึกเดี่ยว Pb(Zr$_{1-x}$Ti$_x$)O$_3$หรือ PZT ที่มีสัดส่วนของ Ti อยู่ที่ x = 0.42 และ x = 0.44โดยเทคนิคสเปก
โทรสโกปีการดูดกลืนรังสีเอ็กซ์ ในช่วงอุณหภูมิ 25-200 องศาเซลเซียสและภายใต้สนามไฟฟ้าที่ 0
กิโลโวลต์ต่อมิลลิเมตร 0.35 กิโลโวลต์ต่อมิลลิเมตร และ 0.7 กิโลโวลต์ต่อมิลลิเมตร โดยผลการ
ทดลองพบว่า การเพิ่มของอุณหภูมิส่งผลต่อการบิดและหดตัวของโครงสร้างเตตระโกนอลใน
แนวแกน c ของผลึกเดี่ยวPZT และจากการศึกษาภายใต้สนามไฟฟ้าพบว่า มีผลทำให้อะตอมของ
ไทเทเนียมขยับออกจากตำแหน่งของศูนย์กลางอะตอมในช่วงค่าสนามไฟฟ้า 0-0.35 กิโลโวลต์ต่อ
มิลลิเมตร ประมาณ 0.006 Å ซึ่งทำการยืนยันผลการทดลองด้วยการคำนวณโครงสร้างเฉพาะ
บริเวณโดยโปรแกรม FEFF 8.2

สาขาวิชาฟิสิกส์   ลายมือชื่อนักศึกษา___โรจน์นภา ธารามาศ___
ปีการศึกษา 2559   ลายมือชื่ออาจารย์ที่ปรึกษา___รัตติกร ยิ้มนิรัญ___
                                                ลายมือชื่ออาจารย์ที่ปรึกษาร่วม___สุภโชค สุ่มนอก___

ROJNAPA THARAMAS : EFFECTS OF TEMPERATURE AND
ELECTRIC FIELD ON LOCAL STRUCTURE OF Pb(Zr,Ti)O$_3$ SINGLE
CRYSTALS STUDIED BY X-RAY ABSORPTION SPECTROSCOPY.
THESIS ADVISOR : ASSOC. PROF. RATTIKORN YIMNIRUN,
Ph.D. 86 PP.

LEAD ZERCONATE TITANATE/SINGLE CRYSTAL/LOCALSTRUCTURE/X-RAY ABSORPTION SPECTROSCOPY

In this work, the local structure of PbZr$_{1-x}$Ti$_x$O$_3$ (x = 0.42 and x = 0.44) single crystals was investigated under various temperatures in the range of 25-200°C and applied electric fields 0kV/mm, 0.35kV/mm and 0.7kV/mm. The X-ray Absorption Near Edge Structure (XANES) spectra were measured at the Ti K-edge and compared with the results from simulations using FEFF8.2 program. From the XAS results, the shifted energy when temperature increased and the spectrum intensities dropped in high temperature indicated that PZT tetragonal phase gradually changed, especially the decrease of the c axis length, to cubic phase. With applied electric field, the integrated intensity of pre-edge XANES spectrum increased, indicating that Ti atom moved off the center approximately 0.006 Å in rang of applied electric field 0-0.35 kV/mm.

School of Physics

Academic Year 2016

Student's Signature _Rojnapa Tharamas_

Advisor's Signature _Rattikorn Yimnirun_

Co-advisor's Signature _สาโรช รุจิรวรรธน์_

ACKNOWLEDGEMENTS

กิตติกรรมประกาศ

โรจน์นภา ธารามาศ

CONTENTS

CONTENTS (Continued)

CONTENTS (Continued)

LIST OF TABLES

Table   **Page**

LIST OF FIGURES

LIST OF FIGURES (Continued)

LIST OF FIGURES (Continued)

LIST OF FIGURES (Continued)

LIST OF FIGURES (Continued)

LIST OF ABBREVIATIONS

AFM	Atomic Force Microscopy
BL5.2	Beamline 5.2
°C	degree Celcius
DOS	Density of State
E_c	coercive field
E_0	Absorption edge
EXAFS	Extended X-ray Absorption Fine Structure
FMS	Full Multiple Scattering
h	Plank's constant
MPB	Morphotropic Phase Boundary
PZT	Lead Zirconate Titanate
SCF	Self Consist Field
SEM	Scanning Electron Microscopy
SLRI	Synchrotron Light Research Institute
XANES	X-ray Absorption Near Edge structure

CHAPTER I

INTRODUCTION

1.1 Background

Currently, the technology has been developed for human living. Smart materials are designed materials that have one or more properties that can be significantly changed in a controlled fashion by external stimuli, such as stress, temperature moisture, pH, electric or magnetic fields. Piezoelectric is one type of smart materials.

$PbZr_{1-x}Ti_xO_3$ solid solution ceramics are undoubtedly the most important ferroelectric materials because of their excellent piezoelectric properties, especially for the compositions close to the so-called morphotropic phase boundary (MPB). They have been used in a wide range of industrial and commercial applications such as peizoelectric actuators, sensors, fuel injectors, sonar, keyboard for the unsighted, etc (Bellaiche, Garcia, 2001). Therefore, a number of investigations have been carried out on the structural evolutions with composition, temperature and the electric field with attempt to explain the excellent piezoelectric response of the MPB compositions. On the other hand, PZT single crystal is extremely difficult to synthesize and very little work has been done on this form of PZT materials. Most of the previous works study the common properties of PZT single crystals, such as standard structural and electrical characterizations and their phase transition behavior. (Xie, 2013) No work has been done on the investigation of their local structure. In this work, we therefor focus on

studying the local structure of $PbZr_xTi_{1-x}O_3$(x=0.42, x=0.44) single crystals under different temperatures and applied electric fields for understanding the phase transition behavior, which in turn will help in clarifying the mechanisms of their ferroelectric properties.

1.2   Review of literatures

1.2.1 Lead Zirconate Titanate (PZT)

Lead zirconate titanate is an intermetallic inorganic compound with the chemical formula $PbZr_xTi_{1-x}O_3$ also called PZT, which is a perovskite material, as shown in Figure 1.1. It shows remarkable piezoelectric effect, meaning that the compound is used in a number of practical applications in the area of electroceramics.
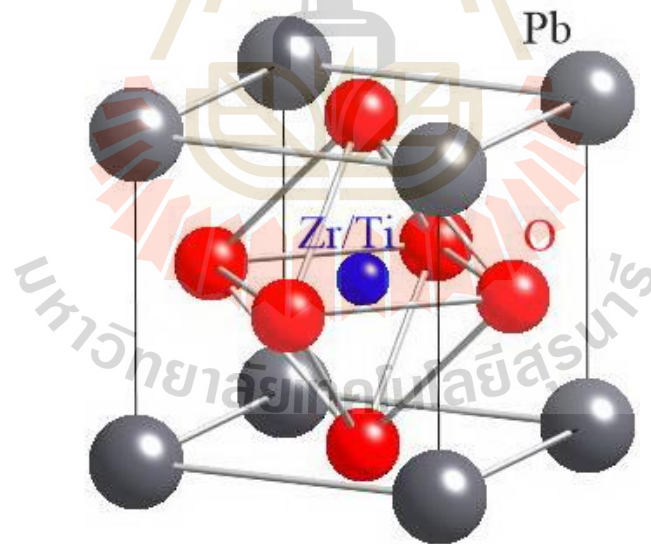
Figure 1.1 The perovskite structure of PZT (cubic).

Pervoskite oxides are the most studied group of ferroelectrics. The perovskite compounds have the general chemical formula ABO_3. In the original phase diagram of $PbZr_{1-x}Ti_xO_3$ which proposed by Jaffe et al. at the room temperature, the

structure of PZT materials is divided into two phases with different symmetries, i.e., the rhombohedral and tetragonal phase, separated by the MPB located at x ~ 0.47 (Xie, 2013) as shown in Figure 1.2. The MPB had long been believed to be a curve connecting the rhombohedral and tetragonal phases in the MPB area, as shown in phase diagram of PZT solid solution (Jaffe et al., 1971).
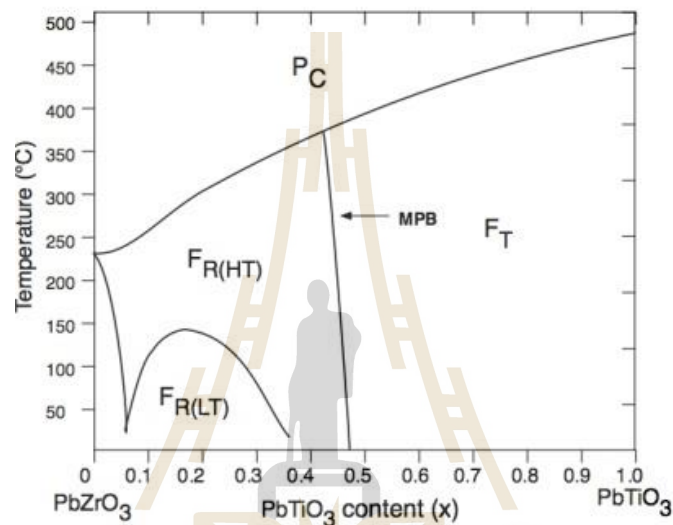
Figure 1.2 Phase diagram of $PbZr_{1-x}Ti_xO_3$ solid solution P_c is paraelectric cubic structure F_R is ferroelectric rhombohedral structure and F_T is ferroelectric tetragonol structure (Xie, 2013).

1.2.2 Effect of electric field on PZT

One of the most important characteristics of single crystal ferroelectrics is the P-E hysteresis loop which displays the variation of polarizations (P) with electric fields (E), as. shown in Figure 1.3. The initial polarization is not zero when no Electric field is applied (point A). With increasing E-field, the polarization increases following the applied electric fields because the Ti^{4+} atoms move along z-axis close to negative charge. The saturated polarization (P_s) is reached when the maximum distance of Ti

displacment (CD). When the E-field is reduced, the total polarization decreases (DE). However, even at zero field xthere still is some remaining polarization or remnant polarization P_r (point E). The opposite E-field required to cancel this polarization is called coercive field E_c (point F) (Xie, 2013).
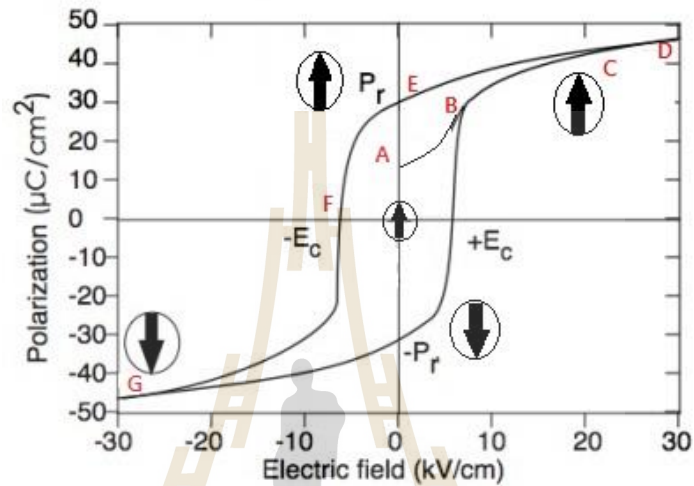
Figure 1.3 Ferroelectric hysteresis loop: variation of polarization as a function of an applied alternative electric field. (Adapted from Xie, 2013)

1.2.3 PZT single crystal

PZT singel crystals have been successfully grown in the Z-G. Ye's Group at Simon Fraser University by a top-seeded solution growth method (Xie, 2013). The availability of PZT single crystals opens the road for the studies of local phases of PZT. Compared with PZT ceramics, these crystals have a higher piezoelectric coefficient (d_{33} > 1700 pC/N) and a larger electromechanical coupling factor (k_{33} > 0.90). Since PZT system has a high T_C ($\approx$ 380°C at x=0.46), it is believed that its single crystals could achieve both excellent piezoelectric properties and high T_C. Even though their properties are superior to those of PZT ceramics, they exhibit some inherent drawbacks,

such as a low MPB phase transition temperature ($T_{MPB} < 100°C$) and a low coercive field ($E_c < 3$ kV/cm), making them unsuitable for high temperature and high field (power) applications.

1.2.4 Ti *K* Pre- edge XANES analysis

The integrated intensity of Ti *K* pre-edge, which is associated with both the quadrupole and the dipole 1s $\longrightarrow$ 3d transition of Ti, reflects the 3*d*-4*p* hybridization for Ti. This hybridization results from displacement of the Ti atom from centro-symmetric position within the oxygen octahedron. Vedrinskii et al. have shown that a contribution to the area under peak X is given by

$$A = \frac{\gamma_s}{3} d_s^2 \tag{1.1}$$

In this equation, d_s is the mean-square displacement of Ti atom from center and a is the average displacement of the oxygen octahedral and A is a peak area. An experimental determination of the constant γ_s by Ravel result in values of 12.5 eV/Å^2 for PbTiO$_3$ with an error bar of about ±3 eV/Å^2 as shown in Figure 1.4.
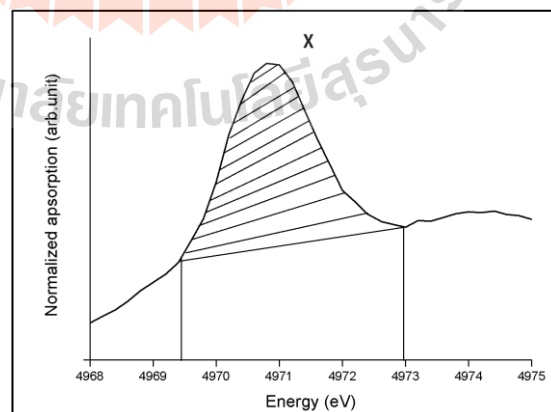
Figure 1.4 The Ti K pre-edge XANES of PbZr$_{1-x}$Ti$_x$O$_3$(x=0.44), showing the calculated area under the spectral peak. (Adapt from Vedrinskii et al., 1998)

1.3 Research objectives

(a) To study the local structure of PZT single crystals by XAS technique.

(b) To investigate the effect of electric field and temperature on the local structure of PZT single crystals.

1.4 Scope and limitation of the study

This study aims to analyze the effects of temperature and electric field on local structure with X-ray absorption spectroscopy technique. We employed XAS technique at Synchrotron Light Research Institute (SLRI, Thailand) to investigate the local structure under various temperatures and applied electric fields in Pb(Zr1-xTix)O3 single crystals with x=0.42 and x=0.44 XANES and EXAFS spectra at the Ti K-edge were measured and compared with simulation done by FEFF8.2 program.

In addition, X-ray Diffraction (XRD), Atomic Force Microscopy (AFM) and Scanning Electron Microscopy (SEM) were also used to investigate the global structure and microstructure, respectively.

CHAPTER II

THEORY AND LITERATURE SURVEY

In this chapter, the experimental techniques used in the thesis work will be reviewed. We will describe the general concept of those techniques and extract the results from experiments. Firstly, the attention was focused to the study of local structure around specific atoms which can be done by using X-ray absorption spectroscopy (XAS) in both X-ray absorption near-edge structure (XANES) and extended X-ray absorption fine structure (EXAFS) regions. Next, scanning electron microscope (SEM) then single X-ray diffraction (SXRD) and atomic force microscopy (AFM) are discussed.

2.1   X-ray absorption spectroscope (XAS)

X-ray absorption spectroscopy (XAS) is a powerful technique for investigating the local distortion due to domain switching in the ferroelectric materials (Cao et al., 2004). It can provide information of the average inter-atomic distance, coordination number and structural disorder. In particular, the low energy region of the spectrum, X-ray Absorption Near-edge Structure (XANES), can be used to determine the specific atom, while the higher energy region, Extended X-ray Absorption Fine Structure (EXAFS), can provide information about the coordination environment for the Ti atoms.

X-ray absorption fine structure (XAFS) is a specific structure observed in XAS. By analyzing the XAFS, information can be acquired on the local structure and on the unoccupied local electronic states. X-rays are electromagnetic wave or photon energies with ranging from~500 eV to 500 keV, or a wavelength from~25 Å to 0.25 Å At this energy regime, light is absorbed by all matter through the photoelectric effect. In this process, an x-ray photon is absorbed by an electron in a tightly bound quantum core level (such as the 1s or 2p level) of an atom (Figure 2.1(a))
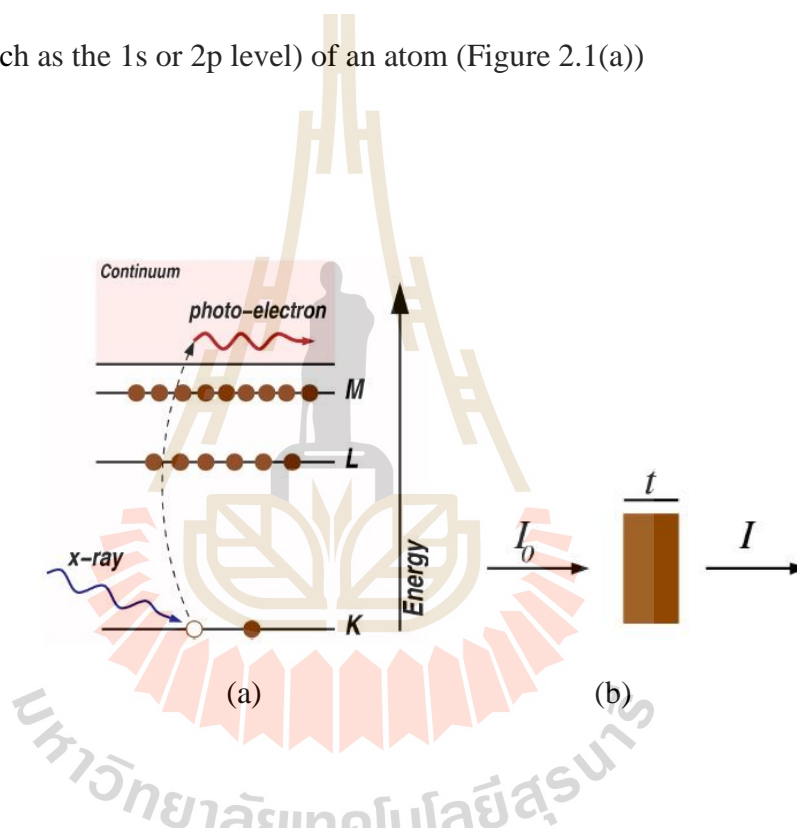
Figure 2.1 (a) The photoelectric effect, in which an X-ray is absorbed and a core level electron is promoted out of the atom. (b) X-ray absorption measurements: An incident beam of monochromatic X-rays of intensity I_0 passes through a sample of thickness t, and the transmitted beam has intensity I (Newville, 2004).

In order for a particular electronic core level to participate in the absorption, the binding energy of this core level must be less than the energy of the incident X - ray. If the binding energy is greater than the energy of the X -ray, the bound electron will not be perturbed from the dell defined quantum state and will not absorb the X- ray. If the binding energy of the electron is less than that of the X-ray, the electron may be removed from its quantum level. In this case, the X-ray is destroyed (i.e., absorbed) and any energy in excess of the electronic binding energy is given to a photo-electron that is ejected from the atom. This process has been well understood for nearly a century (Einstein received the Nobel Prize for describing this effect). The Amplitude modulation has also been used in the non-contact regime to image with atomic resolution by using very stiff cantilevers and small amplitudes in an ultra-high vacuum environment.

The full implications of this process when applied to molecules, liquids, and solids will give rise to XAFS. When discussing X-ray absorption, we are primarily concerned with the absorption coefficient, μ which gives the probability that x-rays will be absorbed according to Beer's Law:

$$I = I_0 e^{-\mu t} \tag{2.1}$$

where I_0 is the X-ray intensity incident on a sample, t is the sample thickness, and I is the intensity transmitted through the sample, as shown in Figure 2.1(b). For X -rays, as for all light, the X -ray intensity is proportional to the number of X -ray photons. At most X-ray energies, the absorption coefficient μ is a smooth function of energy, with a value that depends on the sample density ρ, the atomic number Z, atomic mass A, and the X -ray energy E roughly as

$$\mu \approx \frac{\rho Z^4}{A E^3} \qquad (2.2)$$

The strong dependence of μ on both Z and E is a fundamental property of X-rays, and is the key to why XAS is useful for medical and other imaging techniques including X-ray computed tomography. Due to the Z^4 dependence, the absorption coefficient for O, Ca, Fe, and Pb are very different spanning several orders of magnitude so that good contrast between different materials can be achieved for nearly any sample thickness and concentrations by adjusting the X-ray energy. Figure 2.2 shows the energy-dependence of μ/ρ for O, Fe, Cd, and Pb.
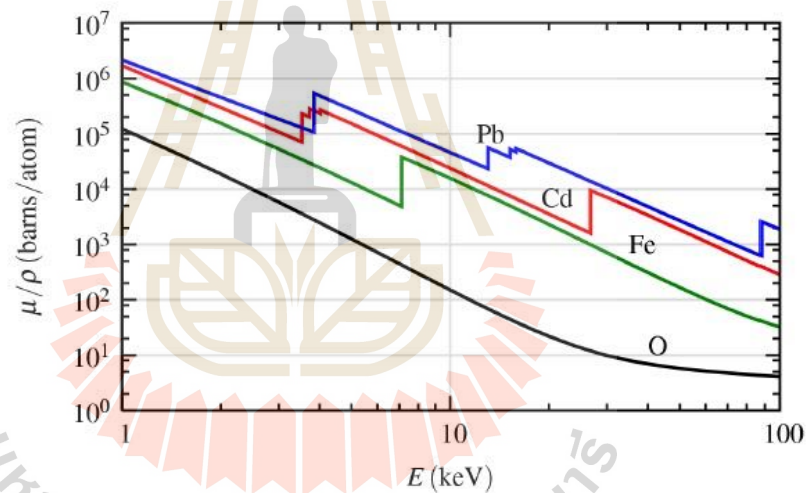
Figure 2.2 The absorption cross-section μ/ρ for several elements over the X -ray energy range of 1 to 100 keV. Notice that there are at least 5 orders of magnitude in variation in μ/ρ and that in addition to the strong energy dependence there are also sharp rises corresponding to the core-level binding energies of the atoms.

There are two main mechanisms for the decay of the excited atomic state following an X-ray absorption event. The first of these is X-ray fluorescence (Figure

2.3), in which a higher energy electron core-level electron fills the deeper core hole, ejecting an x-ray of well-defined energy. The fluorescence energies emitted in this way are characteristic of the atom, and can be used to identify the atoms in a system, and to quantify their concentrations. For example, an L shell electron dropping into the k level gives the $k\alpha$ fluorescence line. The second process for de-excitation of the core hole is the Auger Effect, in which an electron drops from a higher electron level and a second electron is emitted into the continuum (and possibly even out of the sample). In the hard x-ray regime (> 2 keV), X-ray fluorescence is more likely to occur than Auger emission, but for lower energy X-ray absorption, Auger processes dominate. Either of these processes can be used to measure the absorption coefficient μ, though the use of fluorescence is somewhat more common.
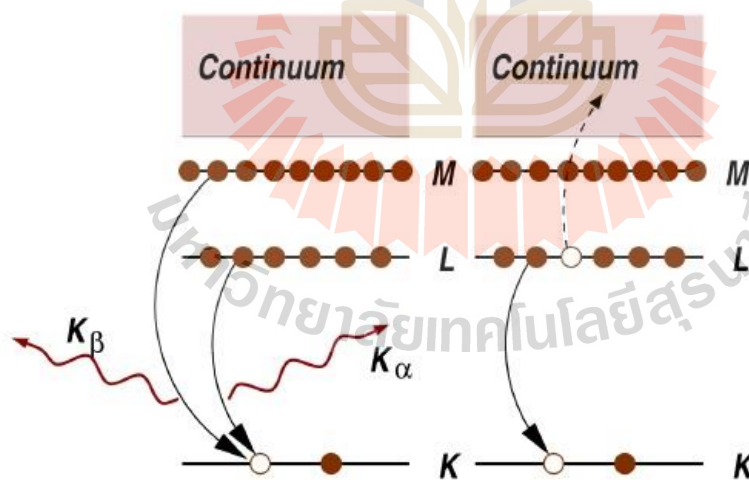
Figure 2.3 Decay of the excited state X-ray fluorescence (left) and the Auger effect (right). In both cases, the probability of emission (X-ray or electron) is directly proportional to the absorption probability.

XAS can be measured either in transmission or fluorescence geometries. We will return to the details of the measurements later. For now it is enough to say that we can measure the energy dependence of the absorption coefficient $\mu(E)$ either in transmission as equation (2.3).

$$\mu(E) = ln(I_0/I) \tag{2.3}$$

Or in X-ray fluorescence as equation (2.4).

$$\mu(E) \propto I_f/I_0 \tag{2.4}$$

where I_f is the monitored intensity of a fluorescence line (or, again, electron emission) associated with the absorption process. A typical XAFS spectrum (measured in the transmission geometry for a powder of FeO is shown in Figure 2.4. The sharp rise in $\mu(E)$, due to the Fe 1s electron level (at 7,112 eV) is clearly visible in the spectra, as are the oscillations in $\mu(E)$, that are the XAFS. As mentioned in the introduction, the XAFS is generally thought of in two distinct portions the XANES typically within 30eV of the main absorption edge, and EXAFS. As we shall, the basic physical description of these two regimes is the same, but some important approximations and limits allow us to interpret the extended spectra in a more quantitative way than is currently possible for the near-edge spectra.

For the EXAFS, we are interested in the oscillations well above the absorption edge and define the EXAFS fine-structure function $\mu(E)$, as

$$x(E) = \frac{\mu(E) - \mu_0(E)}{\Delta\mu_0(E)} \tag{2.5}$$

where $\mu(E)$ is the measured absorption coefficient, $\mu_0(E)$ is a smooth background function representing the absorption of an isolated atom, and $\Delta\mu_0$ is the measured jump in the absorption $\mu(E)$ at the threshold energy E_0. (Figure 2.4 bottom)
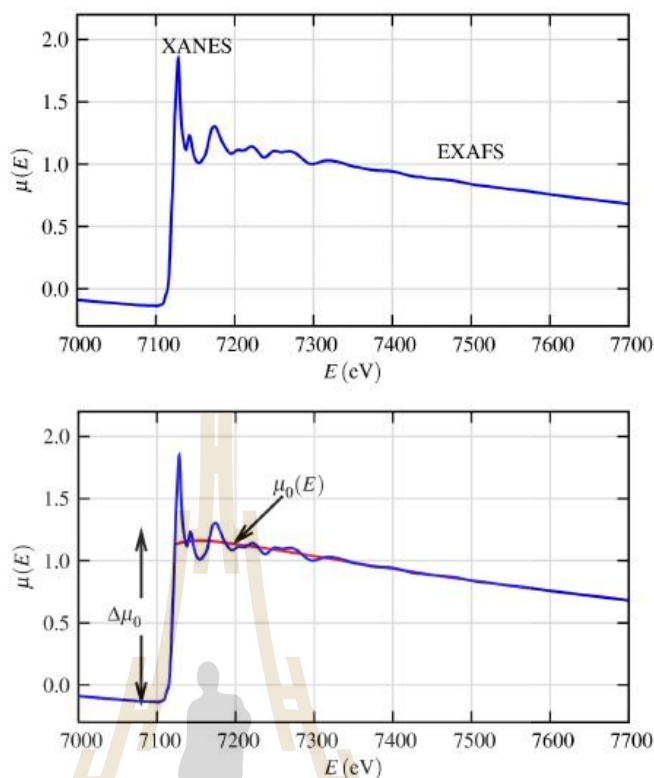
Figure 2.4 XAFS $\mu(E)$ for FeO. On top, the measured XAFS spectrum is shown with the XANES and EXAFS regions identified. On the bottom, $\mu(E)$is shown with smooth background function $\mu_0(E)$ and the edge-step $\Delta\mu_0(E_0)$.

2.1.1 X-ray absorption near edge structure (XANES)

X-ray absorption near edge structure or XANES contains the information about the chemical state of the element, including the oxidation state, and the local geometry of the absorbing atom. XANES structure in an absorption spectrum covers the range between the threshold and the point at which the extended X-ray absorption fine structure (EXAFS) being. XANES comprises that part of the spectrum within about 40-50 eV of the edge.

This region of the absorption spectrum is dominated by multiple scattering of low energy of photoelectron. In addition, there are normally strong features due to

transitions to empty bonding and anti-bonding orbitals in molecular systems or to atomic-like or unoccupied density of state in solid state systems. The combination of these influence mean that XANES is sensitive to the local electronic structure of the absorbing species and the coordination geometry. XANES has most often been used in a fingerprint fashion, with spectra compared to standards to determine the quantity of interest such as the oxidation state of the absorbing element.

The absorption coefficient in equation (2.1) is proportional to the transition rate as given by Fermi's Golden Rule; described by

$$\tilde{\mu}(E) \propto \sum_f \left| \langle f | \hat{\varepsilon} \cdot \bar{r} | i \rangle \right|^2 \delta \left(E_i - E_f + \hbar\omega \right), \qquad (2.8)$$

where $|i\rangle$ is the initial core *ket* state vector, $\langle f|$ is the final *bra* state vector of the excited electron, E is the energy of absorbed x-ray photon, E_i is the energy of initial state, E_f is the energy of final state, $\hbar\omega$ is the energy of x-ray photon energy, $\hat{\varepsilon}$ is the x-ray polarization vector and $\tilde{\mu}(E)$ is absorption coefficient with ignoring of core hole life time and experimental resolution (Ankudinov et al., 1998).

2.1.2 Extended x-ray absorption fine structure (EXAFS)

The extended x-ray absorption fine structure is the oscillating part of the X-ray absorption spectrum that extends to about 1,000 eV above the absorption edge. Analyses of the EXAFS spectrum provide information about the number, species and inter-atomic distances of the neighbors from the absorption atom. EXAFS is a result of the adjustment of the photoelectron final state due to scattering by the surrounding atoms. The final state photoelectron is changed to first order by a single scattering from each surrounding atom. According to quantum theory this photoelectron can be visualized as a wave emitted from the absorber with wavelength λ is given by the de

Broglie relation. In EXAFS region, the momentum of the photoelectron p can be defined by the free electron relation

$$\frac{p^2}{2m} = h\nu - E_0,\tag{2.9}$$

where $h\nu$ is the energy of frequency ν photon, E_0 is the bonding energy of the photoelectron and m is mass of the excited electron.

For a solitary atom the photoelectron can be revealed as an outgoing wave as shown in Figure 2.5 by the solid line of Mg atom. The outing wave is scattered by neighbor that surround the absorbing atom and generate scattered wave, which display by the dashed lines of O atoms. The final state is the superposition of the outgoing and scattered waves. Interference occurs between the outgoing and the backscattered waves and then creates the total amplitude. The total amplitude of the electron wave function would be raised or diminished, respectively, thus altering the possibility of absorption of the x-ray correspondingly. The phase change with the wavelength of the photoelectron depends on the distance between the center atom and backscattering atom. The variation of the backscattering strength as a function of energy of the photoelectron depends on the type of atom doing the backscattering. Thus EXAFS contains information on the atomic surroundings of the center atom.
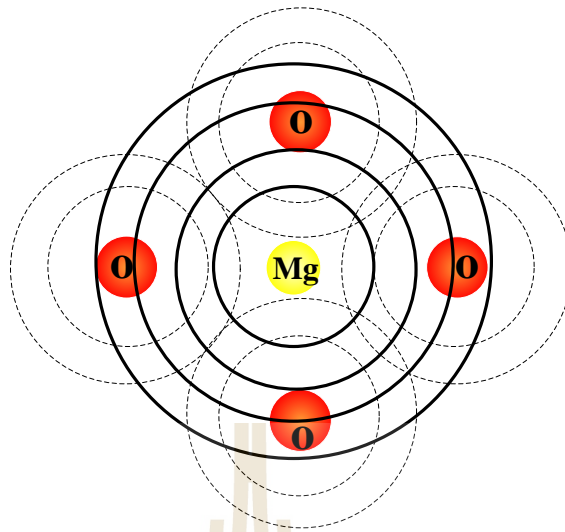
Figure 2.5 Schematic of the radial portion of the photoelectron wave. (Jutimoosik, 2010).

The oscillatory part of the X-ray absorption above a given absorption edge, EXAFS function can be defined by

$$\chi(E) = \frac{\left[\mu(E) - \mu_\circ(E)\right]}{\Delta\mu_\circ}, \tag{2.10}$$

where $\mu(E)$ is the X-ray absorption coefficient, $\mu_0(E)$ is smooth atomic background absorption coefficient.

Furthermore, in the EXAFS analysis $\chi(E)$ could be transformed from E space to k space by the relations $k = \sqrt{2m(E - E_0)/\hbar^2}$. Then the function can be converted from $\chi(E)$ to $\chi(k)$ for general purpose. In theoretical procedure, the $\chi(k)$ can be described by (Wilson et al., 2000)

$$\chi(k) = \sum_j \frac{S_\circ^2 N_j}{k R_j^2} \left| f_j(k, \pi) \right| \sin\left[2kR_j + \varphi_j(k) \right] e^{-2\sigma_j^2 k^2} e^{-2R_j/\lambda(k)}, \tag{2.11}$$

where N_j is the number of neighbor in j^{th} shell of surrounding atoms, k is photoelectron wave vector, f_j is the scattering amplitude, $S_\circ^2(k)$ is the amplitude reduction term due to many-body effect, R_j is radial distance from absorbing atom to j shell, $\lambda(k)$ is electron mean free path, σ_j is the Debye-Waller factor and $\varphi(k)$ accounts for the total phase shift of the curve wave scattering amplitude along the scattering trajectory.

The distance between core atom and backscattering atoms or the path-length change the phase contrasting with the wavelength of photoelectron. Furthermore, different types of surrounding atoms vary the backscattering intensity as a function of photoelectron energy. It is accepted that, by the careful analysis of the EXAFS structure, one can receive significance structural parameters surrounding the center atom.

2.2 X-ray absorption spectrum calculation

2.2.1 FEFF code overview

This thesis, the principle theoretical calculations were performed based on FEFF 8.2 code. This code is developed to primarily calculate X-ray absorption for the FEFF (f_{eff}) project developed by the Department of Physics, University of Washington, Seattle. USA. Apart from XAS spectra calculation, FEFF code can also calculate X-ray natural circular dichroism (XNCD), spin-dependent calculations of X-ray magnetic dichroism (XMCD), nonresonent X-ray emission (XES) and electronic structure including local densities of states (LDOS). FEFF code is written

in ANSI FORTRAN 77 with principle investigator John J. Rehr and co-principle investigator Alexei L. Ankudinov.

FEFF is ab intio self-consistent real space multiple-scattering (RSMS) code for simultaneous calculations of X-ray absorption spectra and electronic structure. The input file "feff.inp" can be created directly form ATOMS code via "atoms.inp" as shown in Figure 2.6.


```
title MgO, sodium chloride structure
space  F M 3 M
a=4.213
rmax=10.0
core=Mg
atom
!at.type    x         y         z
  Mg      0.000     0.000     0.000
  O       0.500     0.500     0.500
```
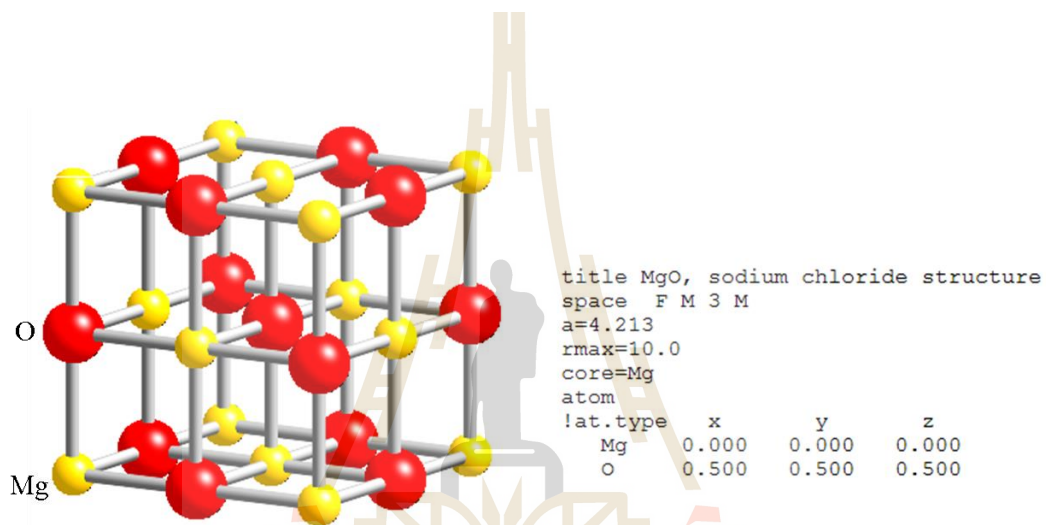
Figure 2.6 Detail of an atoms.inp input file to generate "feff.inp" for FEFF calculation.

```
* This feff.inp file generated by ATOMS, version 2.50
* ATOMS written by and copyright (c) Bruce Ravel, 1992-1999

* -- * -- * -- * -- * -- * -- * -- * -- * -- * -- * -- * -- * -- *
*       total mu =    13646.9 cm^-1, delta mu =    9582.1 cm^-1
*       specific gravity = 3.581, cluster contains  461 atoms.
* -- * -- * -- * -- * -- * -- * -- * -- * -- * -- * -- * -- * -- *
*       mcmaster corrections:  0.00296 ang^2 and  0.210E-04 ang^4
* -- * -- * -- * -- * -- * -- * -- * -- * -- * -- * -- * -- * -- *

TITLE   MgO, sodium chloride structure

EDGE      K
S02       1.0

*         pot   xsph  fms   paths genfmt ff2chi
CONTROL   1     1     1     1     1      1
PRINT     1     0     0     0     0      0

*         r_scf  [ l_scf  n_scf  ca ]
SCF       4.5        0      15   0.1

*         ixc  [ Vr  Vi ]
EXCHANGE  0      0   0

*EXAFS
*RPATH     9.26860

*         kmax  [ delta_k  delta_e ]
XANES     4.0     0.07     0.5
*         r_fms      [ l_fms ]
FMS       8.0          0
*
RPATH     0.10000
*         emin  emax  resolution
*LDOS     -20    20    0.1
POTENTIALS
*   ipot  z [ label   l_scmt  l_fms  stoichiometry ]
     0   12   Mg        -1      -1         0
     1    8   O         -1      -1         1
     2   12   Mg        -1      -1         1

ATOMS
   0.00000     0.00000     0.00000    0   Mg         0.00000
  -2.10650     0.00000     0.00000    1   O          2.10650
   2.10650     0.00000     0.00000    1   O          2.10650
   0.00000     0.00000     2.10650    1   O          2.10650
   0.00000     2.10650     0.00000    1   O          2.10650
   0.00000     0.00000    -2.10650    1   O          2.10650
   0.00000    -2.10650     0.00000    1   O          2.10650
   0.00000     2.10650    -2.10650    2   Mg         2.97904
   0.00000     2.10650     2.10650    2   Mg         2.97904
  -2.10650     2.10650     0.00000    2   Mg         2.97904
                       :
  -6.31950     6.31950     4.21300    2   Mg         9.88036
  -6.31950    -6.31950    -4.21300    2   Mg         9.88036
   6.31950     4.21300     6.31950    2   Mg         9.88036
END
```

Figure 2.7 Detail of a "feff.inp" input file of MgO with Mg as center atom for FEFF calculation.

The suitable commands, parameter and atomic positions for FEFF-XAS spectrum calculations can be edited within the input file named "feff.inp", which is shown in Figure 2.7. This file controlled with some details, for instance the generator of input file and the number of atom which is contain in the cluster. The followed details describe about various card use to assign the steps of calculation. The type of atomic potentials and defined atomic symbols are presented in the next part, and eventually with the locations of the created atoms in the system where the location of center atom is placed at (0,0,0) in (x,y,z) coordination.

2.2.2 XAS Calculation

Calculation of XAS can be carried out with the imaginary part of one-electron Green's function operator (Ankudinov, 1998)

$$G = [E - H]^{-1}, \tag{2.13}$$

where H is the effective one-electron operator Hamiltonian and E is the photoelectron energy. Based on the Green's-function calculation in the complex plane, to explicit equation (2.8) by using spectral representation with Green-function operator, thus the absorption coefficient can be rewritten as

$$\tilde{\mu}(E) \propto -\frac{2}{\pi} \mathrm{Im} \langle i \,|\, \hat{\varepsilon} \cdot \vec{r}\,' G(\vec{r}\,', \vec{r}, E) \hat{\varepsilon} \cdot \vec{r} \,|\, i \rangle, \tag{2.14}$$

where $G(\vec{r}\,', \vec{r}, E) = \langle \vec{r}\,' \,|\, G(E + in) \,|\, \vec{r} \rangle$, $\hat{\varepsilon}$ is the x-ray polarization vector and the parameters denoted with prime is that quantity in final state (Ankudinov, 1998). Furthermore, since only the transition to unoccupied state above Fermi energy are permitted and the effect of core-hole lifetime and experimental resolution are essentially taken in to calculation, the total absorption coefficient should become

$$\mu(E) = \int\limits_{E_F}^{\infty} dE' \tilde{\mu}(E') \frac{\Gamma}{\pi[(E-E')^2 + \Gamma^2]}, \tag{2.15}$$

where Γ is determined by the combined sum of the core-hold life time and experimental resolution, and E_F is Fermi level energy. FEFF code aid scientist to approach the XAS spectra by performing the possibly precise Green's function in $\tilde{\mu}(E)$. For FEFF 8 series, the developers suggested two mains developed feature for XAS calculation. The two main advantage are the approaches of self-consistent field (SCF) and full multiple scattering (FMS).

For XAS calculation (especially XANES), the SCF loop are used to create the SCF potentials and compute the total electron density and Coulomb potential within RSMS Green's-function framework. In FEFF 8.2 code, the SCF potentials are implemented using the spherical or "muffin-tin potential" as illustrated in Figure 2.8. Muffin-tin potential considers the atomic interval potential since a spherical scattering potential center on each atom equal to sum of overlapping potential and has a constant value in the interstitial region between atoms. FMS card will perform the calculation for all possible paths within the defined cluster.

(a)   (b)
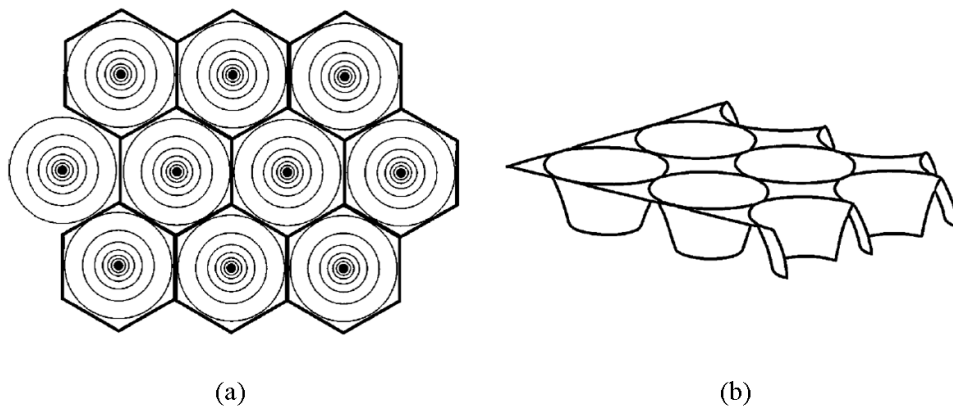
Figure 2.8 Schematic illustration of muffin-tin potential in two dimensions (Rehr and Albers, 2000).

The SCF loop constructs Green's function, which consist of central atom and scattering contribution

$$G(\vec{r},\vec{r}',E) = G^C(\vec{r},\vec{r}',E) + G^{SC}(\vec{r},\vec{r}',E),$$ (2.16)

where $G^C(\vec{r},\vec{r}',E)$ and $G^{SC}(\vec{r},\vec{r}',E)$ are central and scattering contribution, respectively.

XANES calculation can be performed under the defined control cards, most of them are normally used as the defaults, excepting FMS and SCF which are importantly managed. For SCF consideration, the cluster radius is used to define the suitable scattering potential, which usually requires around 30 atoms within the cluster. The appropriate SCF cluster should be the least value that makes the consistent of the spectra presents for saving the computational resources.

For EXAFS calculation, the scattering muffin-tin has less effect to the calculated spectra than at the lower energy region. At EXAFS region, the photoelectron gains larger energy, and then it is less sensitive to the details of

potential between atoms. Therefore, SCF calculation may not be essential in the EXAFS calculation.

2.3 Single crystal X-ray diffraction (SXRD)

The most common experimental method of obtaining a detailed structure of a molecule, that allows a resolution of individual atoms, single crystal X-ray diffraction (SXRD) is performed by analyzing the pattern of X-rays diffracted by an ordered array of many identical molecules (single crystal). Many pure compounds, from small molecules to organometallic complexes, proteins, and polymers, solidify into crystals under the proper conditions. When solidifying into the crystalline state, these individual molecules typically adapt one of only a few possible 3D orientations. When a monochromatic X-ray beam is passed through a single crystal, the radiation interacts with the electrons in the atoms, resulting in scattering of the radiation to produce a unique image pattern. Multiple images are recorded, with an area X-ray detector, as the crystal is rotated in the X-ray beam. Computationally intensive analysis of a set images results in a solution for the 3D structure of the molecule.

X-ray diffractometers consist of three basic elements, an X-ray tube, a sample holder, and an X-ray detector. X-rays are generated in a cathode ray tube by heating a filament to produce electrons, accelerating the electrons toward a target by applying a voltage, and impact of the electrons with the target material. When electrons have sufficient energy to dislodge inner shell electrons of the target material, characteristic X-ray spectra are produced. These spectra consist of several components, the most common being K_α and K_β. K_α consists, in part, of $K_{\alpha 1}$ and $K_{\alpha 2}$. $K_{\alpha 1}$ has a slightly shorter wavelength and twice the intensity as $K_{\alpha 2}$. The specific wavelengths are

characteristic of the target material. Filtering, by foils or crystal monochrometers, is required to produce monochromatic X-rays needed for diffraction. $K_{\alpha 1}$ and $K_{\alpha 2}$ are sufficiently close in wavelength such that a weighted average of the two is used. Molybdenum is the most common target material for single-crystal diffraction, with MoK_{α} radiation = 0.7107Å. These X-rays are collimated and directed onto the sample. When the geometry of the incident X-rays impinging the sample satisfies the Bragg Equation, constructive interference occurs. A detector records and processes this X-ray signal and converts the signal to a count rate which is then output to a device such as a printer or computer monitor. X-rays may also be produced using a synchrotron, which emits a much stronger beam.
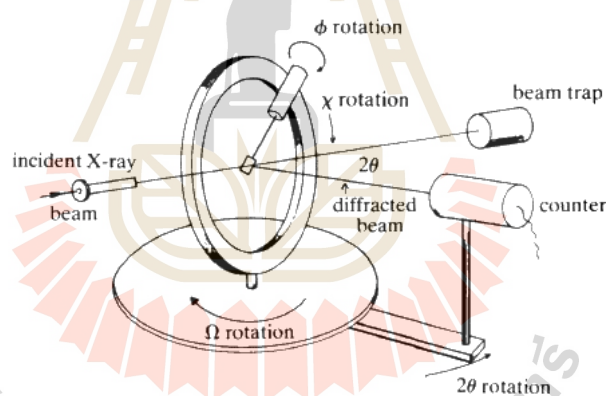
Figure 2.9 Schematic of 4-circle diffractometer, the angles between the incident ray, the detector and the sample.

Single-crystal diffractometers use either 3 or 4 circle goniometers. These circles refer to the four angles ($2\theta, \chi, \varphi$, and Ω) that define the relationship between the crystal lattice, the incident ray and detector. Samples are mounted on thin glass fibers which are attached to brass pins and mounted onto goniometer heads. Adjustment of

the X, Y and Z orthogonal directions allows centering of the crystal within the X-ray beam.
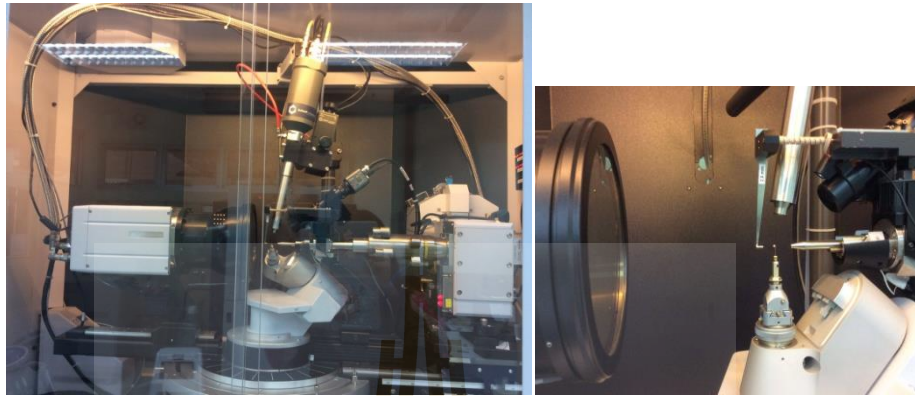
Figure 2.10 (a) single crystal X-ray Diffraction set up at The Center for Scientific and Technological Equipment. (b) Schematic of 4-circle diffractometer, the angles between the incident ray, the detector and the sample.

X-rays leave the collimator and are directed at the crystal. Rays are either transmitted through the crystal, reflected off the surface, or diffracted by the crystal lattice. A beam stop is located directly opposite the collimator to block transmitted rays and prevent burn-out of the detector. Reflected rays are not picked up by the detector due to the angles involved. Diffracted rays at the correct orientation for the configuration are then collected by the detector. Modern single-crystal diffractometers use CCD (charge-coupled device) technology to transform the X-ray photons into an electrical signal which are then sent to a computer for processing.

2.3.1 Sample selection and preparation

Samples for single-crystal diffraction should be selected from unfractured, optically clear crystals. This can be determined by viewing the samples under crossed polars on a petrographic microscope. Crystals can be broken off a larger sample and

the best fragment selected. Samples should be between 30 and 300 microns, with ideal crystals averaging 150-250 microns in size. To minimize absorption affects, equant crystals are preferred. Spherical crystals can be created using a small, air-powered crystal tumbler, however easily cleaved minerals can break during this process. Therefore, minerals lacking cleavage are the best choice for this step. If the sample is in equant, this must be corrected for during absorption corrections to the data.
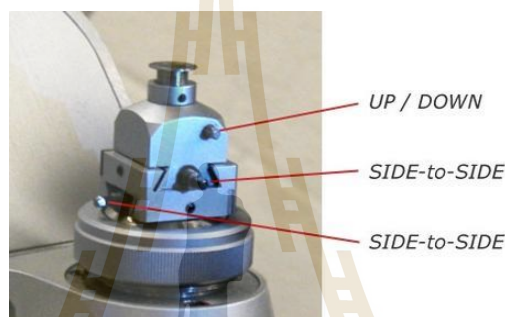
Figure 2.11 Goniometer head.

Samples are mounted on the tip of a thin glass fiber using an epoxy or cement. Care should be taken to use just enough epoxy to secure the sample without embedding it in the mounting compound. The fiber may be ground to a point to minimize absorption by the glass. This fiber is attached to a brass mounting pin, usually by the use of modeling clay, and the pin is then inserted into the goniometer head.The goniometer head and sample are then affixed to the diffractometer. Samples can be centered by viewing the sample under an attached microscope or video camera and adjusting the X,Y and Z directions until the sample is centered under the cross-hairs for all crystal orientations.

2.3.2 Data collection

Once the crystal is centered, a preliminary rotational image is often collected to screen the sample quality and to select parameters for later steps. An automatic collection routine can then be used to collect a preliminary set of frames for determination of the unit cell. Reflections from these frames are auto-indexed to select the reduced primitive cell and calculate the orientation matrix (which relates the unit cell to the actual crystal position within the beam). The primitive unit cell is refined using least-squares and then converted to the appropriate crystal system and Bravias lattice. This new cell is also refined using least-squares to determine the final orientation matrix for the sample.

After the refined cell and orientation matrix have been determined, intensity data is collected. Generally this is done by collecting a sphere or hemisphere of data using an incremental scan method, collecting frames in 0.1° to 0.3° increments (over certain angles while others are held constant). For highly symmetric materials, collection can be constrained symmetrically to reduce the collection time. Data is typically collected between 4° and 60° 2θ for molybdenum radiation. A complete data collection may require anywhere between 6-24 hours, depending on the specimen and the diffractometer. Exposure times of 10-30 seconds per frame for a hemisphere of data will require total run times of 6-13 hours. Older diffractometers with non-CCD detectors may require 4-5 days for a complete collection run.

2.3.3 Corrections

After the data have been collected, corrections for instrumental factors, polarization effects, X-ray absorption and (potentially) crystal decomposition must be applied to the entire data set. This integration process also reduces the raw frame data

to a smaller set of individual integrated intensities. These correction and processing procedures are typically part of the software package which controls and runs the data collection.

2.3.4 Structure solution

Solution of the phase problem leads to the initial electron density map. Elements can be assigned to intensity centers, with heavier elements associated with higher intensities. Distances and angles between intensity centers can also be used for atom assignment based on likely coordination. If the sample is of a known material, a template may be used for the initial solution. More information about structure solution and refinement can be found on the single-crystal structure refinement page.

2.3.5 Structure refinement

Once the initial crystal structure is solved, various steps can be done to attain the best possible fit between the observed and calculated crystal structure. The final structure solution will be presented with an R value, which gives the percent variation between the calculated and observed structures. The single-crystal structure refinement page provides further information on the processes and steps involved in refining a crystal structure.

2.4 Scanning electron microscopy (SEM)

SEM is a type of electron microscope that produces images of a sample by scanning it with a focused beam of electrons. The electrons interact with atoms in the sample, producing various signals that can be detected and that contain information about the sample's surface topography and composition.

The schematic diagram of scanning electron microscope is shown in Figure 2.12. The SEM generates a beam of incident electrons in an electron column above the sample chamber. The electrons are produced by a thermal emission source, such as a heated tungsten filament, or by a field emission cathode. The energy of the incident electrons can be as low as 100 eV or as high as 30 keV depending on the evaluation objectives. The electrons are focused into a small beam by a series of electromagnetic lenses in the SEM column. Scanning coils near the end of the column direct and position the focused beam onto the sample surface. The electron beam is scanned in a raster pattern over the surface for imaging. The beam can also be focused at a single point or scanned along a line for x-ray analysis. The beam can be focused to a final probe diameter as small as about 10 Å. when the electron beam strikes a specimen, a large number of signals are generated. These signals include secondary electrons, backscattered electrons, characteristic x-ray, cathodoluminescence and transmitted electrons, as shown in Figure 2.13.
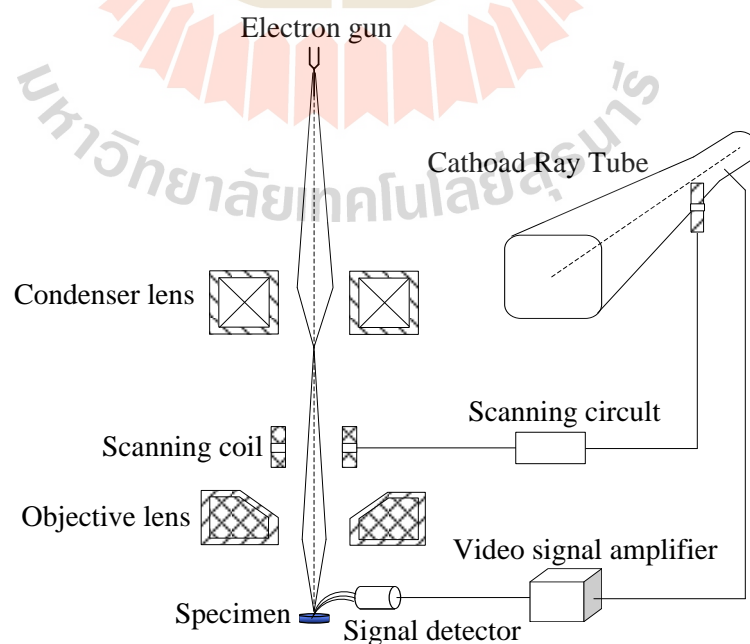
Figure 2.12 Principles schematic illustration of SEM (JEOL, Ltd., 1989).
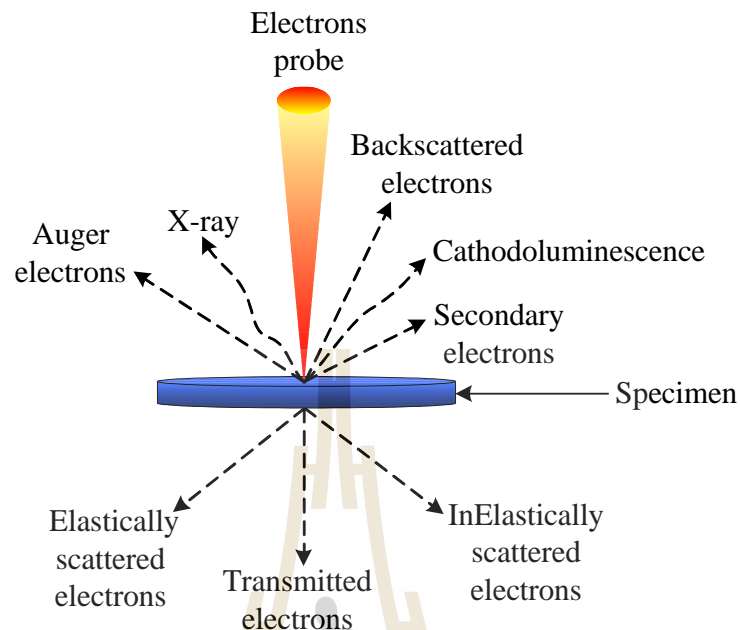
Figure 2.13 schematic diagrams of signals in SEM.

There are four significant signals to be use in SEM:

    1) Secondary Electrons (SE) are emitted lower-energy electrons, which can be formed by inelastic collisions with the nucleus where substantial energy loss occurs or by the ejection of loosely bound electrons from the sample atoms. The energy of secondary electrons is typically 50 eV or less. The topography of surface features influences the number of electrons that reach the secondary electron detector from any point on the scanned surface. This local variation in electron intensity creates the image contrast that reveals the surface morphology. The secondary electron image resolution for an ideal sample is about 3.5 nm for a tungsten-filament electron source SEM or 1.5 nm for field emission SEM.

2) Backscattered electrons are high-energy electrons that are ejected by an elastic collision of an incident electron, typically with a sample atom's nucleus. These high-energy electrons can escape from much deeper than secondary electrons, so surface topography is not as accurately resolved as for secondary electron imaging. The production efficiency for backscattered electrons is proportional to the sample material's mean atomic number, which results in image contrast as a function of composition, mean that higher atomic number material appears brighter than low atomic number material in a backscattered electron image. The optimum resolution for backscattered electron imaging is about 5.5 nm.

3) Characteristic x-rays are generated when the electron beam interacts with the inner shell electrons of the specimen atoms by inelastic scattering with enough energy to excite inner shell electrons to outer shell orbitals, leaving inner-shell vacancies. As outer-shell electrons fall to the various inner shell orbitals, characteristic amounts of energy are generated that are a function of the target element and the type of orbital decay. These characteristic x-ray are used to identify the component and measure the plenty of elements in the sample.

4) Cathodoluminescence (CL), the emission of light when atoms excited by high-energy electrons come back to their ground state. In the SEM, CL detectors either collect all light emitted by the specimen, or can analyse the wavelengths emitted by the specimen and display an emission spectrum or an image of the distribution of cathodoluminescence emitted by the specimen in real colour.

To create an SEM image, the incident electron beam is scanned in a raster pattern across the sample's surface. The emitted electrons are detected for each position in the scanned area by an electron detector. The intensity of the emitted electron signal is displayed as brightness on a cathode ray tube (CRT). By synchronizing the CRT scan to that of the scan of the incident electron beam, the CRT display represents the morphology of the sample surface area scanned by the beam. Magnification of the CRT image is the ratio of the image display size to the sample area scanned by the electron beam.

Two electron detector types are predominantly used for SEM imaging. Scintillator type detectors (Everhart-Thornley) are used for secondary electron imaging. This detector is charged with a positive voltage to attract electrons to the detector for improved signal to noise ratio. Detectors for backscattered electrons can be scintillator types or a solid-state detector. The SEM column and sample chamber are at a moderate vacuum to allow the electrons to travel freely from the electron beam source to the sample and then to the detectors. High-resolution imaging is done with the chamber at higher vacuum, typically from 10^{-5} to 10^{-7} Torr. Imaging of nonconductive, volatile, and vacuum-sensitive samples can be performed at higher pressures.

2.5 Atomic force microscopy (AFM)

AFM or scanning-force microscopy (SFM) is a type of scanning probe microscopy (SPM), with demonstrated resolution on the order of fractions of a nanometer, more than 1000 times better than the optical diffraction limit. The

information is gathered by feeling or touching the surface with a mechanical probe. Piezoelectric elements that facilitate tiny but accurate and precise movements on (electronic) command enable very precise scanning.

The AFM consists of a cantilever with a sharp tip (probe) at its end that is used to scan the specimen surface the block diagram of AFM shown in Figure 2.14. The cantilever is typically silicon or silicon nitride with a tip radius of curvature on the order of nanometers. When the tip is brought into proximity of a sample surface, forces between the tip and the sample lead to a deflection of the cantilever according to Hooke's law (Cappella and Dietler, 1999.) Depending on the situation, forces that are measured in AFM include mechanical contact force, van der Waals forces, capillary forces, chemical bonding, electrostatic forces, magnetic forces (see magnetic force microscope, MFM), Casmir forces, salvation, etc. Along with force, additional quantities may simultaneously be measured through the use of specialized types of probes. The AFM can be operated in a number of modes, depending on the application. In general, possible imaging modes are divided into static (also called contact) modes and a variety of dynamic (non-contact or "tapping") modes shown in Figure 2.15 where the cantilever is vibrated or oscillated at a given frequency (Binnig et al., 1986).
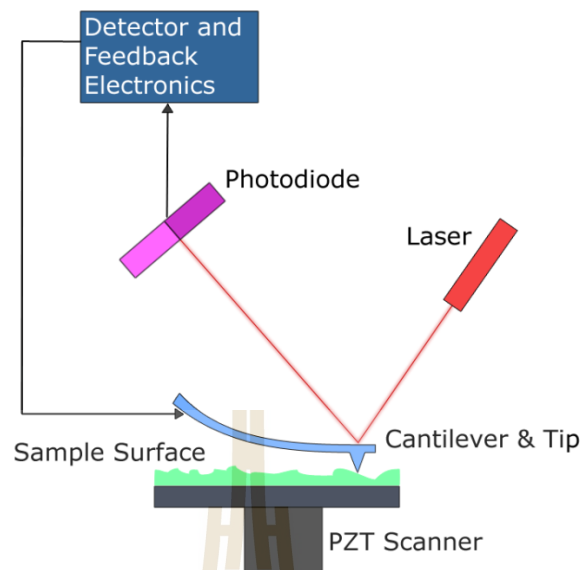
Figure 2.14 Block diagram of atomic-force microscope using beam deflection detection. As the cantilever is displaced via its interaction with the surface, so too will the reflection of the laser beam be displaced on the surface of the photodiode.

AFM operation is usually described as one of three modes, according to the nature of the tip motion: contact mode, also called static mode (as opposed to the other two modes, which are called dynamic modes); tapping mode, also called intermittent contact, AC mode, or vibrating mode, or, after the detection mechanism, amplitude modulation AFM; non-contact mode or again after the detection mechanism, frequency modulation AFM.
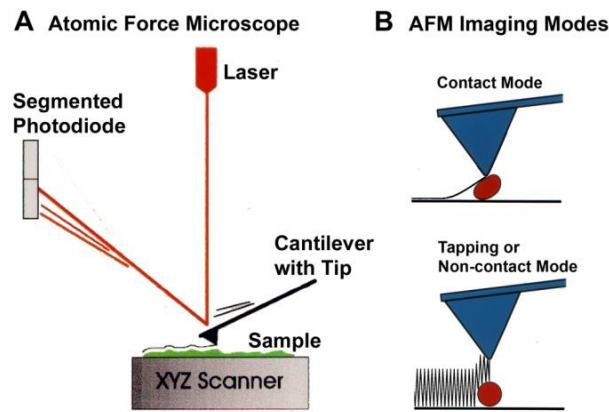
Figure 2.15 Diagram of atomic-force microscope for contact mode and non-contact mode.

2.5.1 Contact mode

In contact mode, the tip is dragged across the surface of the sample and the contours of the surface are measured either using the deflection of the cantilever directly or, more commonly, using the feedback signal required to keep the cantilever at a constant position. Because the measurement of a static signal is prone to noise and drift, low stiffness cantilevers (i.e. cantilevers with a low spring constant, k) are used to achieve a large enough deflection signal while keeping the interaction force low. Close to the surface of the sample, attractive forces can be quite strong, causing the tip to "snap-in" to the surface. Thus, contact mode AFM is almost always done at a depth where the overall force is repulsive, that is, in firm "contact" with the solid surface.

2.5.2 Tapping mode

In ambient conditions, most samples develop a liquid meniscus layer. Because of this keeping the probe tip close enough to the sample for short-range forces to

become detectable while preventing the tip from sticking to the surface presents a major problem for non-contact dynamic mode in ambient conditions. Dynamic contact mode (also called intermittent contact, AC mode or tapping mode) was developed to bypass this problem (Zhong et al., 1993). Nowadays, tapping mode is the most frequently used AFM mode when operating in ambient conditions or in liquids.

In tapping mode, the cantilever is driven to oscillate up and down at or near its resonance frequency. This oscillation is commonly achieved with a small piezo element in the cantilever holder, but other possibilities include an AC magnetic field (with magnetic cantilevers), piezoelectric cantilevers, or periodic heating with a modulated laser beam. The amplitude of this oscillation usually varies from several nm to 200 nm. In tapping mode, the frequency and amplitude of the driving signal are kept constant, leading to constant amplitude of the cantilever oscillation as long as there is no drift or interaction with the surface. The interaction of forces acting on the cantilever when the tip comes close to the surface, Van der Waals forces, dipole-dipole interactions, electrostatic forces, etc. cause the amplitude of the cantilever's oscillation to change (usually decrease) as the tip gets closer to the sample. This amplitude is used as the parameter that goes into the electronic servo that controls the heightof the cantilever above the sample. The servo adjusts the height to maintain a set cantilever oscillation amplitude as the cantilever is scanned over the sample. A tapping AFM image is therefore produced by imaging the force of the intermittent contacts of the tip with the sample surface (Geisse and Nicholas, 2009). Although the peak forces applied during the contacting part of the oscillation can be much higher

than typically used in contact mode, tapping mode generally lessens the damage done to the surface and the tip compared to the amount done in contact mode. This can be explained by the short duration of the applied force, and because the lateral forces between tip and sample are significantly lower in tapping mode over contact mode. Tapping mode imaging is gentle enough even for the visualization of supported lipid bilayers or adsorbed single polymer molecules (for instance, 0.4 nm thick chains of synthetic polyelectrolytes) under liquid medium. With proper scanning parameters, the conformation of single molecules can remain unchanged for hours and even single molecular motors can be imaged while moving.

2.5.3 Non-contact mode

In non-contact atomic force microscopy mode, the tip of the cantilever does not contact the sample surface. The cantilever is instead oscillated at either its resonant frequency (frequency modulation) or just above (amplitude modulation) where the amplitude of oscillation is typically a few nanometers (<10 nm) down to a few picometers (Gross et al., 2009). The van der Waals forces, which are strongestfrom 1 nm to 10 nm above the surface, or any other long-range force that extends above the surface acts to decrease the resonance frequency of the cantilever. This decrease in resonant frequency combined with the feedback loop system maintains a constant oscillation amplitude or frequency by adjusting the average tip-to-sample distance. Measuring the tip-to-sample distance at each (x,y) data point allows the scanning software to construct a topographic image of the sample surface. Non-contact mode AFM does not suffer from tip or sample degradation effects that are sometimes observed after taking numerous scans with contact AFM. This makes

non-contact AFM preferable to contact AFM for measuring soft samples, e.g. biological samples and organic thin film. In the case of rigid samples, contact and non-contact images may look the same. However, if a few monolayers of adsorbed fluid are lying on the surface of a rigid sample, the images may look quite different. An AFM operating in contact mode will penetrate the liquid layer to image the underlying surface, whereas in non-contact mode an AFM will oscillate above the adsorbed fluid layer to image both the liquid and surface.

Schemes for dynamic mode operation include frequency modulation where a phase-locked loop is used to track the cantilever's resonance frequency and the more common amplitude modulation with a servo loop in place to keep the cantilever excitation to a defined amplitude. In frequency modulation, changes in the oscillation frequency provide information about tip-sample interactions. Frequency can be measured with very high sensitivity and thus the frequency modulation mode allows for the use of very stiff cantilevers. Stiff cantilevers provide stability very close to the surface and, as a result, this technique was the first AFM technique to provide true atomic resolution inultra-high vacuum conditions (Giessibl and Franz, 2003).

In amplitude modulation, changes in the oscillation amplitude or phase provide the feedback signal for imaging. In amplitude modulation, changes in the phase of oscillation can be used to discriminate between different types of materials on the surface. Amplitude modulation can be operated either in the non-contact or in the intermittent contact regime. In dynamic contact mode, the cantilever is oscillated such that the separation distance between the cantilever tip and the sample surface is modulated.

2.6 Previous work

In previous work, the original phase diagram of PZT proposed by Jaffe et al., the low temperature ferroelectric is divided into two phases with different symmetries, i. e., the rhombohedral phase and the tetragonal phase, separated by the MPB located at x ~ 0.47. The MPB had long been believed to be a curve connecting the rhombohedral and tetragonal phases until Noheda et al. (2000) using high-resolution synchrotron x-ray diffraction, found the monoclinic M_A phase with a Cm symmetry within the MPB. Similar intermediate monoclinic phase Pm was discovered in the MPB of relaxor based solid-solution PMN-PT and PZN-PT (Kiat et al., 2002). Detailed Rietveld refinement of neutron powder diffraction data was performed on PZT ceramics and it was found that the MPB region of PZT is actually a mixture of R3m, Cm and P4mm phases shown in Figure 2.16.
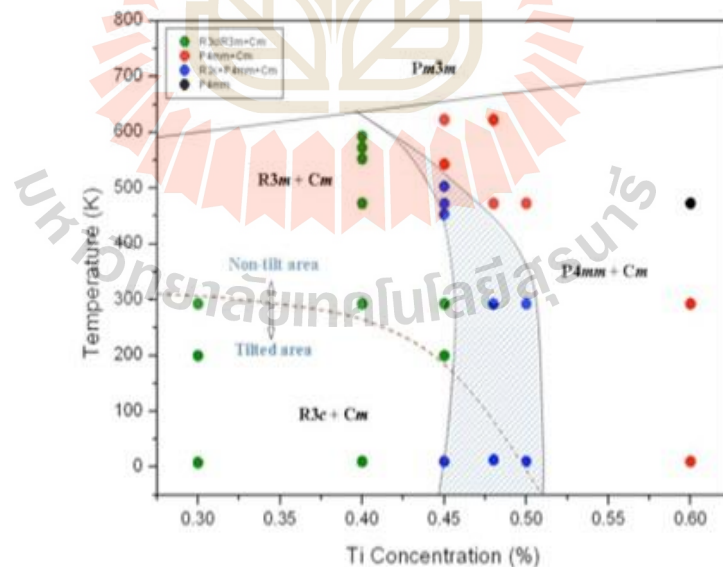
Figure 2.16 Recently updated phase diagram of PZT showing the coexistence of different phases in the areas around MPB (Zhang et al., 2011).

Neutron and X-ray powder diffraction measurements provide information on the average structure. To study the local structure of PZT, it is important to employ local probing techniques. X-ray absorption spectroscopy (XAS) turns out to be an essential tool for that purpose as it provides a direct probe of local structure.

In 2013, PZT ceramic Studied by using in-situ XAS technique to investigate unit cell distortion with in- situ static electrical loading (W. Kempet et al., 2013). The in-situ technique was applied to determine the change of Ti atom position of PZT ceramic under an electrical field.
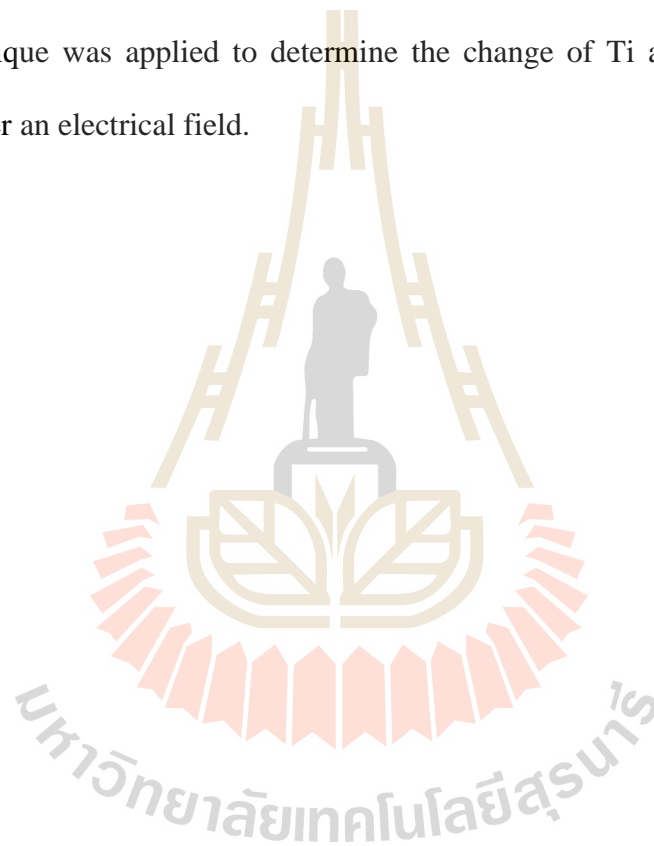
CHAPTER III

RESEARCH METHODOLOGY

This chapter will describe the methods used in this thesis. XAS, SEM, SXRD and AFM are discussed in details.

3.1   X-ray absorption Spectroscopy experimental set up

The X-ray absorption spectroscopy experiment is commonly accomplished at a synchrotron radiation source, due to high intensity and energy alterable competency of generated x-ray photon, and the competency to obtain the continuous absorption spectrum over extensive energy range. In general, there are three types of x-ray absorption measurements: transmission-mode XAS, fluorescence-mode XAS and electron-yield XAS as schematic illustration shown in Figure 3.1.
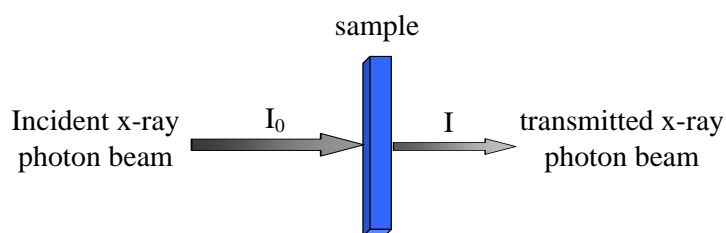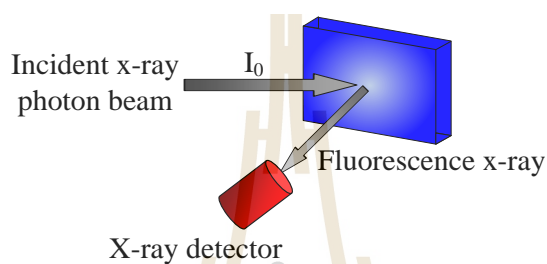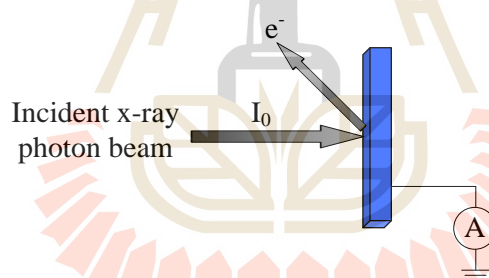
Figure 3.1 The three modes of XAS measurement (a) transmission mode, (b) fluorescence mode and (c) electron yield (Jutimoosik, 2010).

In transmission mode XAS, after the energy of x-ray photons being changed by x-ray double crystals monochromator, the intensities of incident X-ray photon beam (I_0) and the transmitted X-ray photon beam (I) are measured by ionization chambers as shown in Figure 3.2. In this mode, we make sure the x-ray photon beam

is well-aligned on the sample. The x-ray absorption can be extracted based on equation (2.1). The experimental set up of XAS experimental station at XAS beam line, Siam Photon Laboratory, SLRI is shown in Figure 3.3.
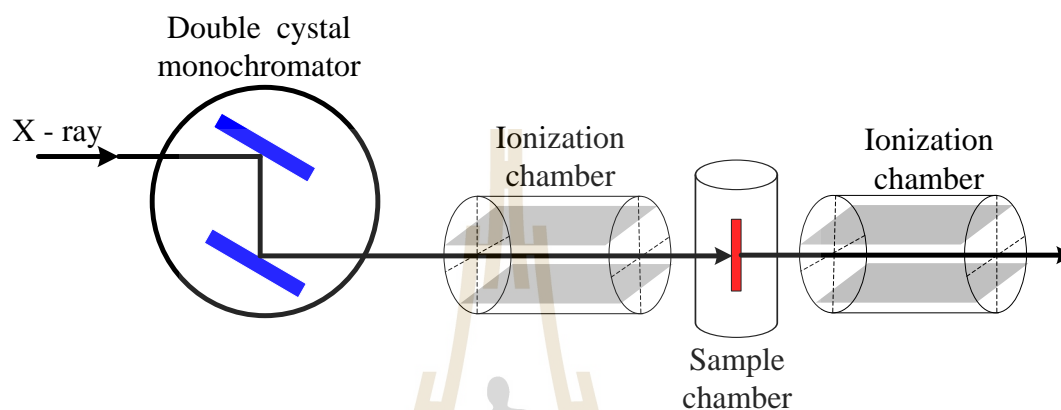
Figure 3.2 Schematic illustration of the experimental setup of transmission-mode X-ray absorption spectroscopy.

Figure 3.3 XAS experimental which BL5.2 set up at the Siam Photon Laboratory, Synchrotron Light Research Institute.

Other than the transmission mode, the fluorescence mode and the electron yield are also competent for the measurement of the absorption coefficient. In the x-ray absorption phenomena, where x-ray photon knock out an electron from the inner shell an electron from higher energy level will cascade down to fill in the hole and discharging radiation of energy, the discharged energy x-ray photon will be released as demonstrated in Figure 3.4(a) and the fluorescence x-ray can be detected. In addition, de-excitation can cause the Auger effect, where the electron reduce to lower energy state, a second electron can be excited to the continuum state and perhaps go out from the sample as shown in Figure 3.4(b), and then we can be detected it by using the electron-yield XAS detectors.

For fluorescence mode, we measure the intensities of incident x-ray photon beam and the fluorescence x-ray that are emitted following the x-ray absorption. Usually the fluorescence detector is placed at 90° to the incident x-ray photon beam in the horizontal plane, with the sample at an angle (usually 45°) with respect to the beam. Fluctuations in the number of elastically scattered x-ray are a significant source of noise in fluorescence XAS, so the position of the detector is selected to minimize the elastically scattered radiation by exploiting the polarization of the x-ray beam. In case of electron yield, we measure the electrons that are emitted from the surface of the sample. The relative short path length (≈ 1000 Å) makes the technique surface-sensitive, which can be beneficial if one is interested in near-surface phenomena. It also can be beneficial for avoiding "self absorption" effect that occurs in fluorescence mode. However, both modes are instantly equivalent to the absorption ability of the sample. Hence, the three techniques are alterable for the study of the structure of material using the absorption ability of the sample.
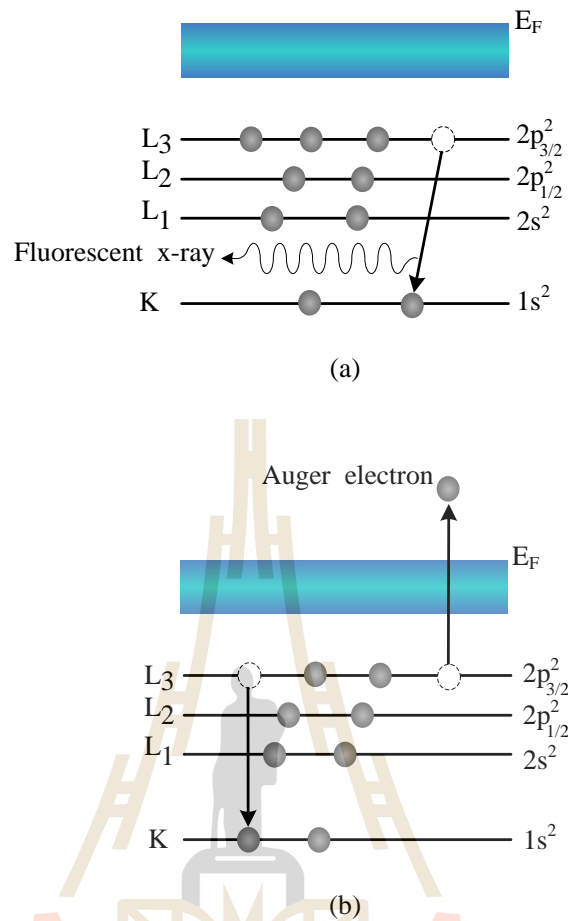
Figure 3.4 The excited state (a) x-ray fluorescence and (b) the Auger effect (adapted from Koningsberger and Prins, 1988).

The experiments use small ceramic plate heater to increase temperature of the materials. When we apply the voltage into MMCPH as shown in Figure 3.5, the plate is heating up, then placed it between the metal plate's (Figure 3.6) and heat insulation plate. Then we attached a sample to be measured on a metal plate and leads to the linear drive to measure the XANES spectrum further. The materials were measured at room temperature, after that we increased temperature to 100°C and 200°C. Thermocouple was connected to the sample holder to measure the temperature of the metal plate.
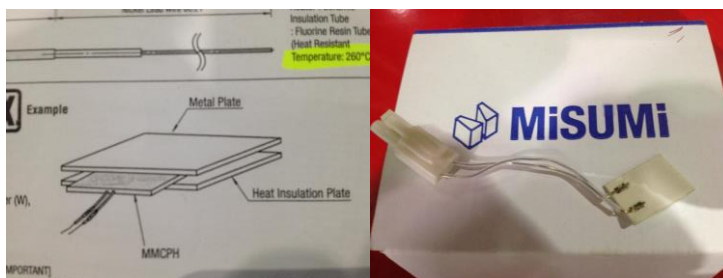
Figure 3.5 Small ceramic plate heater.

Figure 3.6 Metal plate and heat insulation plate.

To perform the *in-situ* XAS under high voltage load, the custom-build sample chamber was designed as shown in Figure 3.7. This special-designed chamber can be subjected to ±1.5 kV and aligned into the incident X-ray beam direction. During the experiment, the sample was installed in the acrylic sample holder. The copper was used as electrical connectors connected to a high voltage power supply (20/20 Trek). The step DC of 0 kV/mm, 0.35 kV/mm and 0.7 kV/mm with the current limit of 20 mA was applied to the sample.
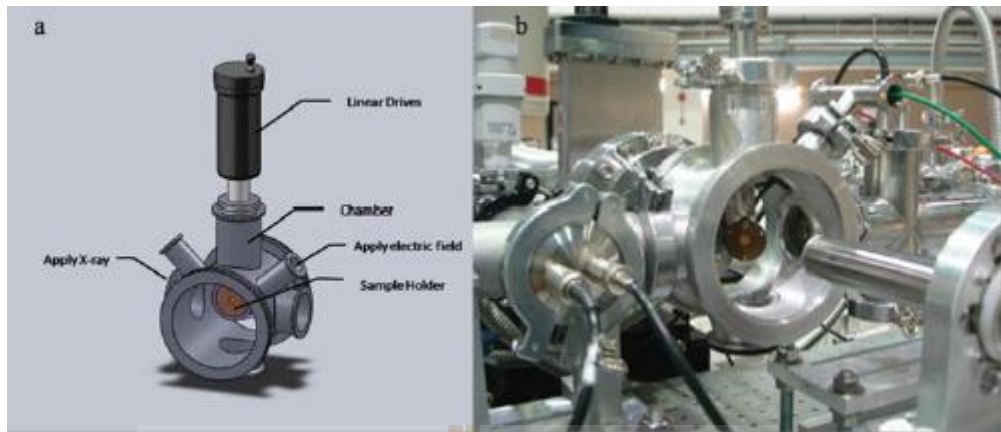
Figure 3.7 (a) Schematic drawing of a sample holder (b) The experiment setting up (W. Kempet et al., 2013).

3.1.1 Ti K Pre- edge XANES analysis

The integrated intensity of Ti K pre-edge, which is associated with both the quadrupole and the dipole 1s $\longrightarrow$ 3d transition of Ti, reflects the 3d-4p hybridization for Ti. This hybridization results from displacement of the Ti atom from centro-symmetric position within the oxygen octahedron. Shown that a contribution to the area under peak X is given by

$$A = \frac{\gamma_s}{3} d_s^2 \tag{3.1}$$

In this equation, d_s is the mean-square displacement of Ti atom from center and a is the average displacement of the oxygen octahedral and A is a peak area. An experimental determination of the constant γ_s by Ravel resulted in values of 12.5 eV/Å^2 for PbTiO$_3$ with an error bar of about ± 3 eV/Å^2 (Vedrinskii et al., 1998) as shown in Figure 3.8.
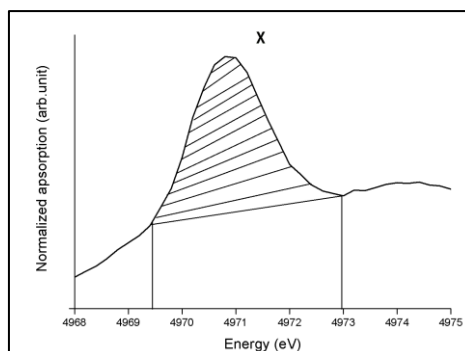
Figure 3.8 The Ti K pre-edge XANES of $PbZr_{1-x}Ti_xO_3(x=0.44)$, showing the calculated area under the spectral peak. (Adapt from Vedrinskii et al., 1998)

3.1.2 XAS measurement

XAS spectra were obtained at the XAS facility (BL-5.2) of the Siam Photon Laboratory, Synchrotron Light Research Institute, Nakhon Ratchasima, with the storage ring running at 1.2 GeV and beam current of 80 - 130 mA during the measurement. XAS measurement was performed in the fluorescence mode using and Ge (220) monochromators for Ti K-edge XAS spectra. The spectra were collected for the K-edges of Ti (4966 eV). XANES were collected at an energy step of 0.2 eV and times step 3 seconds.

PZT single crystals with x=0.42 were heated at room temperature, 100°C and 200°C with Ti K-edge (4966 eV). XANES measurement. The electric field applied on the PZT x=0.44 sample at 0 kV/mm, 0.35 kV/mm, 0.7 kV/mm, 0.35 kV/mm return, 0 kV/mm return and -0.35 kV/mm until -0.7 kV/mm. XANES and EXAFS spectra at the Ti K-edge XAS analysis were done using IFEFFIT package and FEFF 8.2 code. The other techniques to measure the characteristic of PZT single crystal include SEM, SXRD, AFM.

3.2   Single crystal X-ray diffraction

Single-crystal X-ray diffraction is a non-destructive analytical technique which provides detailed information about the internal lattice of crystalline substances, including unit cell dimensions, bond-lengths, bond-angles, and details of site-ordering. Directly related is single-crystal refinement, where the data generated from the X-ray analysis is interpreted and refined to obtain the crystal structure. The interaction of the incident rays with the sample produces constructive interference (and a diffracted ray) when conditions satisfy Bragg's Law ($n\lambda = 2dsin\theta$). This law relates the wavelength of electromagnetic radiation to the diffraction angle and the lattice spacing in a crystalline sample. These diffracted X-rays are then detected, processed and counted. By changing the geometry of the incident rays, the orientation of the centered crystal and the detector, all possible diffraction directions of the lattice should be attained. PZT single crystals were subjected to SXRD at The Center for Scientific and Technological Equipment, Suranaree University of Technology with the X-ray wavelength 1.54184 Å.
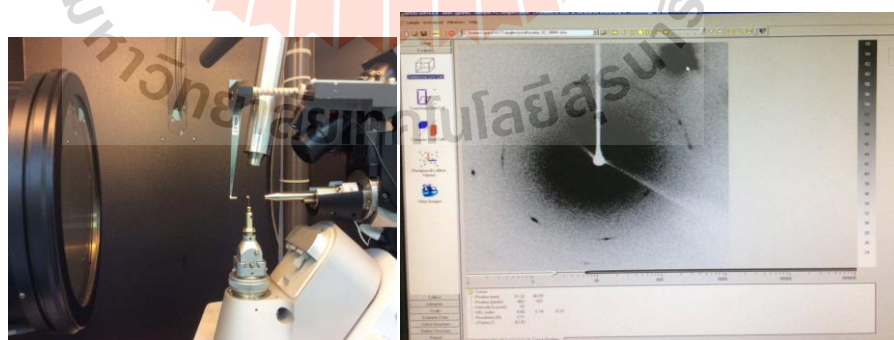
(a)   (b)

Figure 3.9 (a) single crystal X-ray Diffraction set up at The Center for Scientific and Technological Equipment. (b) The fewer the spot of XRD pattern for crystal PZT (x=0.44) in single crystal XRD harvest spot program.

3.3   Scanning electron microscope

PZT single crystals were subjected to SEM at The Center for Scientific and Technological Equipment, Suranaree University of Technology, which is a type of electron microscope that produces images of a sample by scanning it with a focused beam of electrons. The electrons interact with atoms in the sample, producing various signals that can be detected and that contain information about the sample's surface topography and composition.

Figure 3.10 SEM setting up at The Center for Scientific and Technological Equipment, Suranaree University of Technology.

3.4   Atomic force microscopy (AFM)

PZT single crystal with x=0.42 were heated at 100°C, 200°C, 300°C, 400°C and return at room temperature again. The results compose of three signals; the image of topography, EFM phase and EFM amplitude.

Electrostatic Force Microscopy (EFM) is a technique used to map electric properties on a sample surface by measuring the electrostatic force between the surface and a biased AFM cantilever. EFM images contain information about electric properties such as the surface potential and charge distribution of a sample surface. EFM measurements follow the same procedure. For EFM, the sample surface properties would be electrical properties and the interaction force will be the electrostatic force between the biased tip and sample.

However, in addition to the electrostatic force, the Van der Waals forces between the tip and the sample surface are always present. The magnitude of these Van der Waals forces change according to the tip-sample distance, and are therefore used to measure the surface topography.

Hence, the obtained signal contains both information of surface topography (called Topo signal) and information of surface electrical property (called EFM signal) generated by the Van der Waals and electrostatic forces, respectively. The key to successful EFM imaging lies in the separation of the EFM signal from the entire signal. EFM modes can be classified according to the method used to separate the EFM signal.
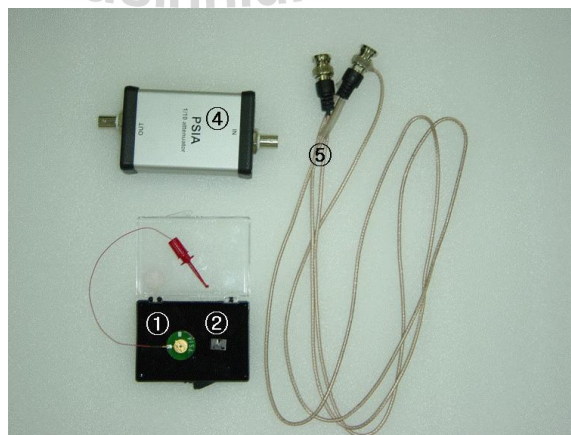
Figure 3.11 Required Component.

3.4.1 Devices for standard EFM mode

1. Place the SR830 Lock-in Amplifier so that the cables can extend easily between it and the XE controller, and so that controls are accessible

2. Connect the five BNC cables included in the Enhanced EFM toolkit as follows. The connections are diagrammed in Figure 3.11.

a. Connect a BNC cable between the Sine Out connector on the Lock-in Amplifier and the connector labeled Ext. Tip Bias on the back panel of the XE controller. This cable carries the AC bias signal applied to the cantilever. DC bias signal also can be applied to the cantilever from the tip bias control window in the XEP software.
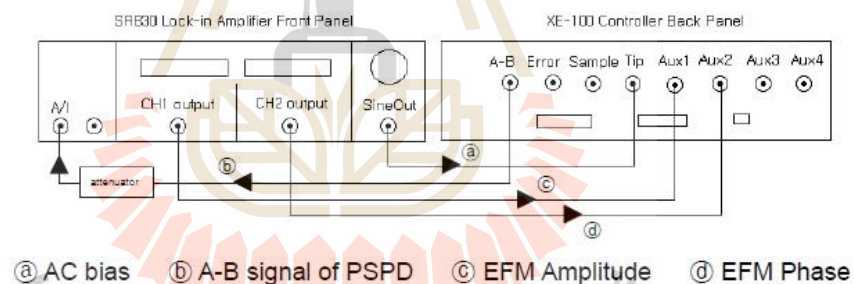
Figure 3.12 BNC Cable Connections.

b. Connect a BNC cable between the connector labeled A-B on the back panel of the XE controller and a connector of the attenuator labeled "in". Then connect a BNC cable between an input connector of the Lock-in Amplifier (labeled A/I on the front panel of the SR830) and a connector of the attenuator labeled "out". The function of the attenuator is to reduce the signal from the PSPD which has maximum output voltage of 10V by 1/10 before sending it to the A/I connector which can only

receive maximum 1V input. This cable carries the total cantilever deflection signal, also called the A-B signal, from the instrument to the Lock-in Amplifier.

c. Connect a BNC cable between a CH1 (CH2) output connector of the Lock-in amplifier and the connector labeled Aux ADC1 (Aux ADC2) on the XE controller. The connector labeled Aux ADC1 (ADC2) on the XE controller is an input that connects to the EFM Amplitude (Phase) signal channel of XEP software in Enhanced EFM. Thus later, you will set up the Lock-in Amplifier so that the output of CH1 (CH2) is the amplitude (phase) of the signal with a frequency that matches the reference frequency ω.

3. Turn on the Lock-in Amplifier and set the following.

a.Time constant: 1 to 3 ms

b. Signal input: A

c. Couple: AC d. Ground: Ground

e. CH1 Display: X(R) f. CH1 Output: Display
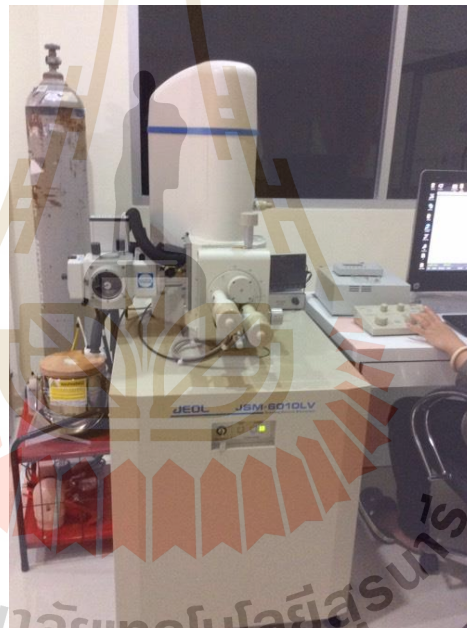
g. CH2 Display: ω h. CH2 Output: Display

i. Trig: SINE j. Source: INT
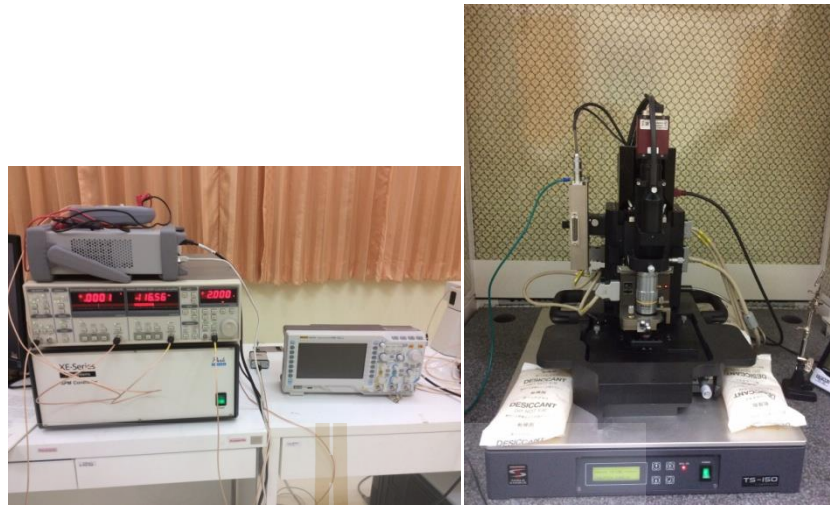
Figure 3.13 EFM set up at the Center for Scientific and Technological Equipment, Suranaree University of Technology.

3.4.2 Preparing the Tip and Sample

1. Attach the sample to the sample disk by using an adhesive. Electro-conductive adhesive such as silver paste is recommended.

2. Sample bias will be applied through the sample holder and can be controlled by changing the Sample bias value in the XEP software.

Setting the sample bias value to zero will have same effect as grounding the sample. But if needed, connect the ground wire or the proper external voltage line to the sample.

    a.   Mount the sample disk on the magnetic sample holder.

    b. If you have connected the ground wire or external voltage line to the sample, connect the other end of the wire or line to the proper grounding or voltage source, respectively. Any conducting part on the SPM body such as clip of the scanner connection cable, SPM body, stage, etc can be used as grounding.

    c.   Mount the tip as it is done in NC-AFM.

CHAPTER IV

RESULTS AND DISCUSSION

In this chapter, the local structural study of $Pb(Zr_{1-x}Ti_x)O_3$ (with x=0.44 and x=0.42) single crystals will be studied and discussed using XAS, SXRD, SEM and AFM. XAS is a powerful tool for resolving the local structure surrounding Ti atoms in PZT crystals. The local structure of Ti and atoms in the PZT crystals, when applying temperature and electric field will be shown in this chapter.

4.1   Effect of the temperature on local structure

The XANES results of PZT with x = 0.42 at room temperature, 100°C and 200°C are shown in the Figure 4.1. The integrated intensity of peak A relate to electron 1s excite to 3d orbital at 4,970 eV which does not allow by select on rules of dipole transitions. However, the bonding effects of TiO_6 allow the electron 1s excite to 3d orbitals which is described by Ligand field theory (Griffith and Orgel, 1957). The integrated intensity of peak B corresponds to electron 1s to 4p level at 4,983 eV and carries out from absorber atoms, after then occur the back scattering with neighbor atoms of spherical electron wave which are including intensities of peak C and D at 4,990 and 4,995 eV, respectively.
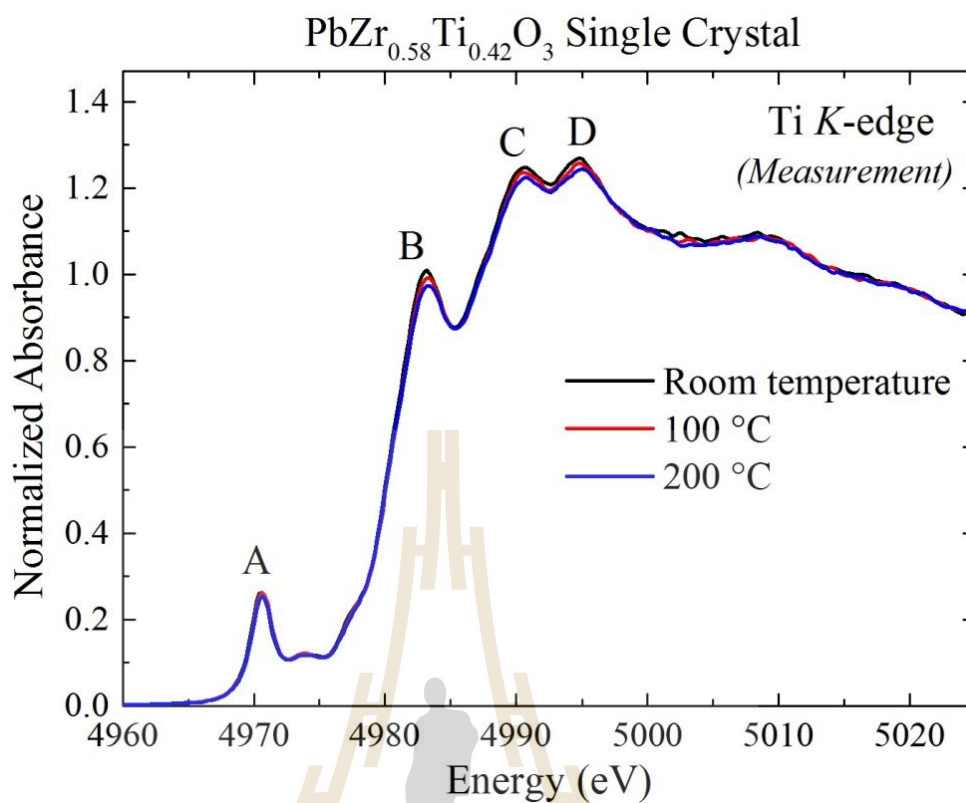
Figure 4.1 Normalized Ti *K*-edge XANES spectra of PZT single crystal with x = 0.42

at room temperature, 100°C and 200°C.
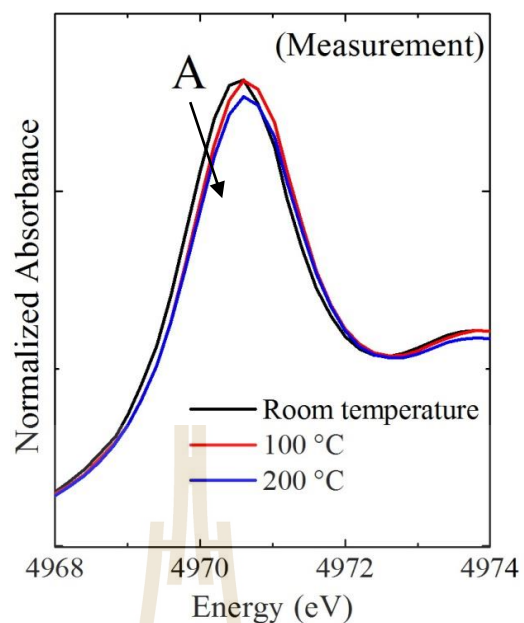
Figure 4.2 Normalized XANES spectrams of PZT with x=0.42 showing the intensities of peak A in range of photon energy from 4,968 eV to 4,974 eV with various temperatures.

Figure 4.2 shows the intensity of peak A related to electron 1s excite to 3d levels.The area of peak A for all spectra is not changed with temperatures at 100°C and 200°C. However, it exhibits a slight energy shift which is caused by the heating into sample. Possiblely, it means that the temperature affects the 3d level of Ti atoms.
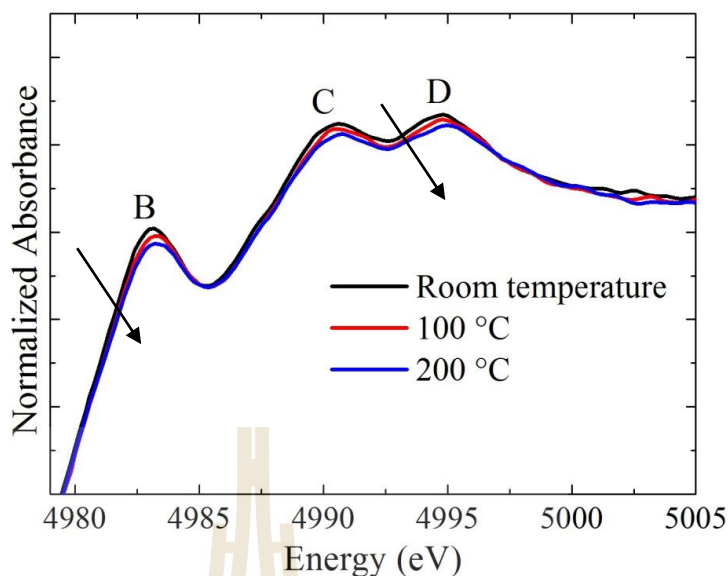
Figure 4.3 Normalized XANES spectra of PZT with x=0.42 in the energy 4,980 eV to 5,005 eV to show the intensity of peak B, C and D.

Figure 4.3 shows the intensities of peak B, C and D at various temperatures. The spectrum changes slightly in peak B, while the spectrum at 100°C is similar to the spectrum at 200°C, indicating that the electrons 1s excite to 4p level and carries out of the absorber atoms. The intensities of the peak C and D have not changed. However, we must do some calculation to support the experiment and confirm the results of temperature effect to the atom moving to the more cubic structure.

This work refers to XAS result of Jiang et al. (2015) to study the temperature dependence of the Yb L_3-edge. PFY-XAS spectra for YNP and YNA were also measured from room temperature to 10 K. With decreasing temperature, the intensity of the Yb^{2+} component increases at the expense of the Yb^{3+} component in both compounds, indicating enhanced valence fluctuations at low temperatures. It can be seen that the temperature affects the peak intensities, and in turn affects the local structure too.
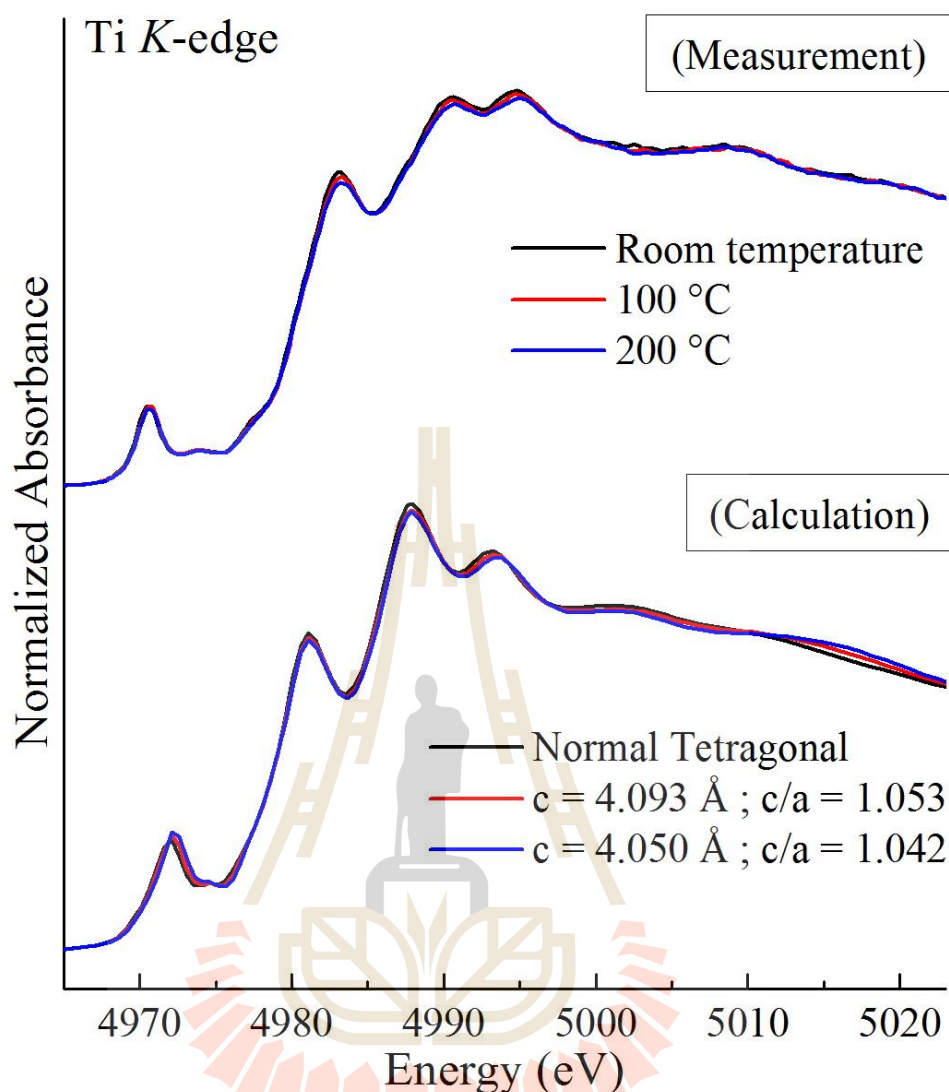
Figure 4.4 Calculated Ti K-edge XANES spectra at the shrunken c axis parameter of tetragonal structure when the temperature increases.

Figure 4.4 shows calculated Ti K-edge XANES spectra of the c axis parameter of PZT tetragonal structure at a tetragonal structure with c=4.139, c=4.039 Å and c=4.050 Å. As compared with the measurements when the temperature has increased, the c parameter shrinks towards more of the cubic phase in PZT phase diagram (Xie, 2013).
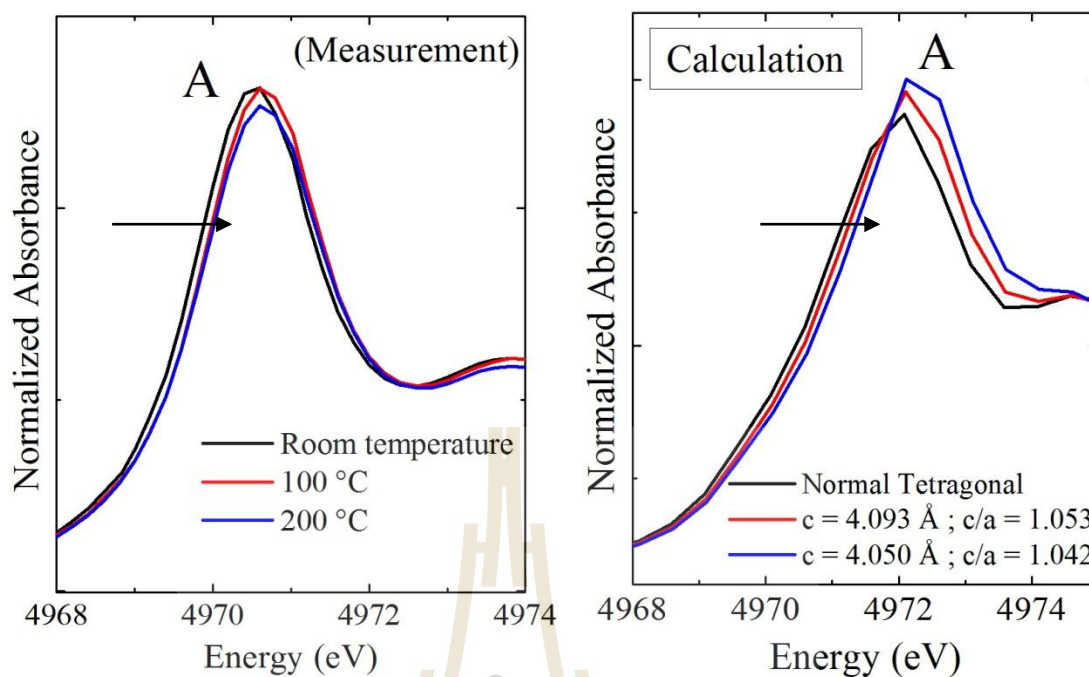
Figure 4.5 Normalized XANES spectra of PZT with x=0.42 showing the intensities of peak A in range of photon energy from 4,968 eV to 4,974 eV at various temperature as compared with the calculation.

The results of the shifted energy in the peak A as temperature increases are confirmed by this calculation, as shown in Figure 4.5. While the intensities of peak B, C and D also dropped in high temperature, related with a shrink of the length of c axis in PZT tetragonal structure. This result indicates that PZT tetragonal phase gradually changes, especially the decrease of the c axis length, to cubic phase when the temperature increases.
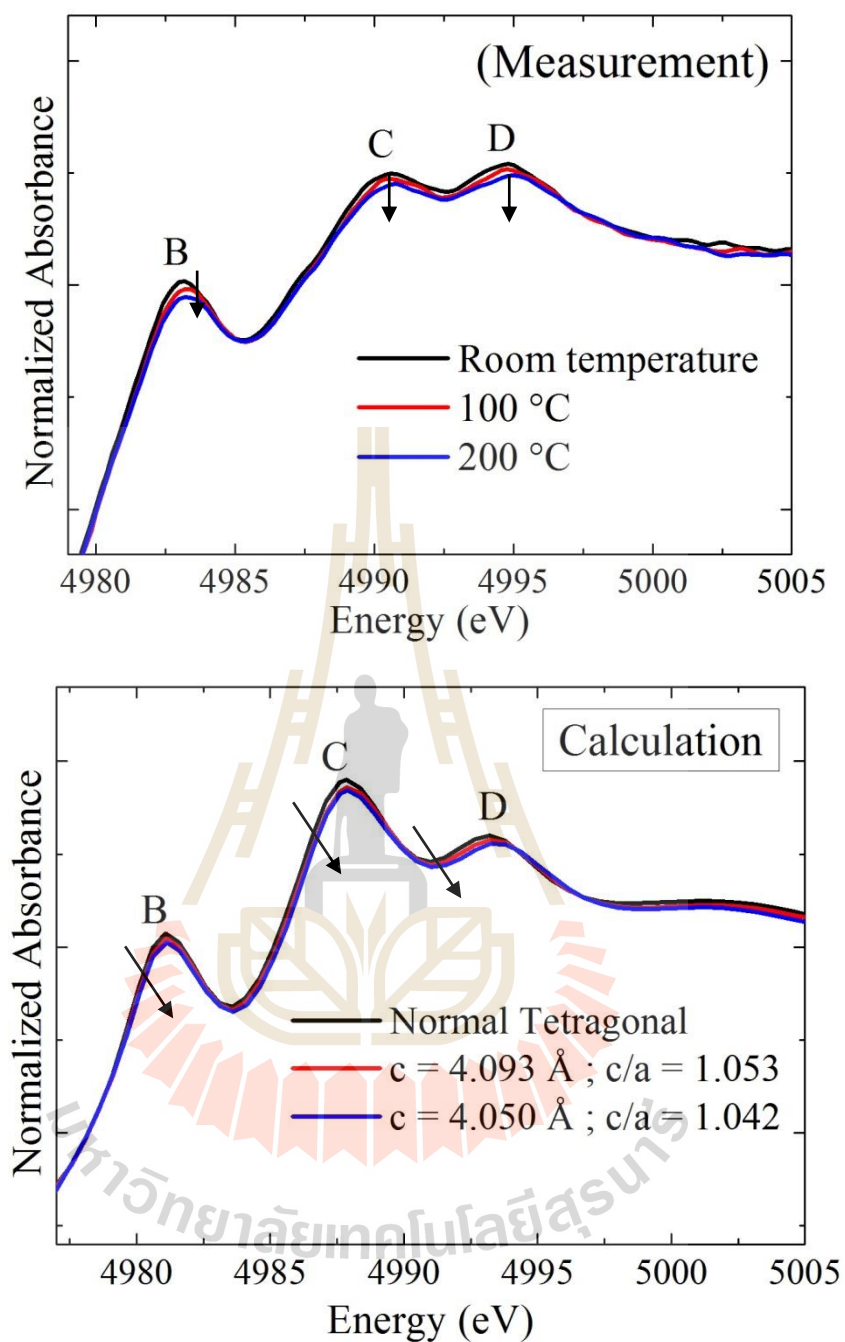
Figure 4.6 Normalized XANES spectras of PZT with x=0.42 showing the intensities of

peak B, C and D in range of photon energy from 4,980 eV to 5,005 eV at various

temperature and compared with the calculation.

4.2 Effect of applied electric field.
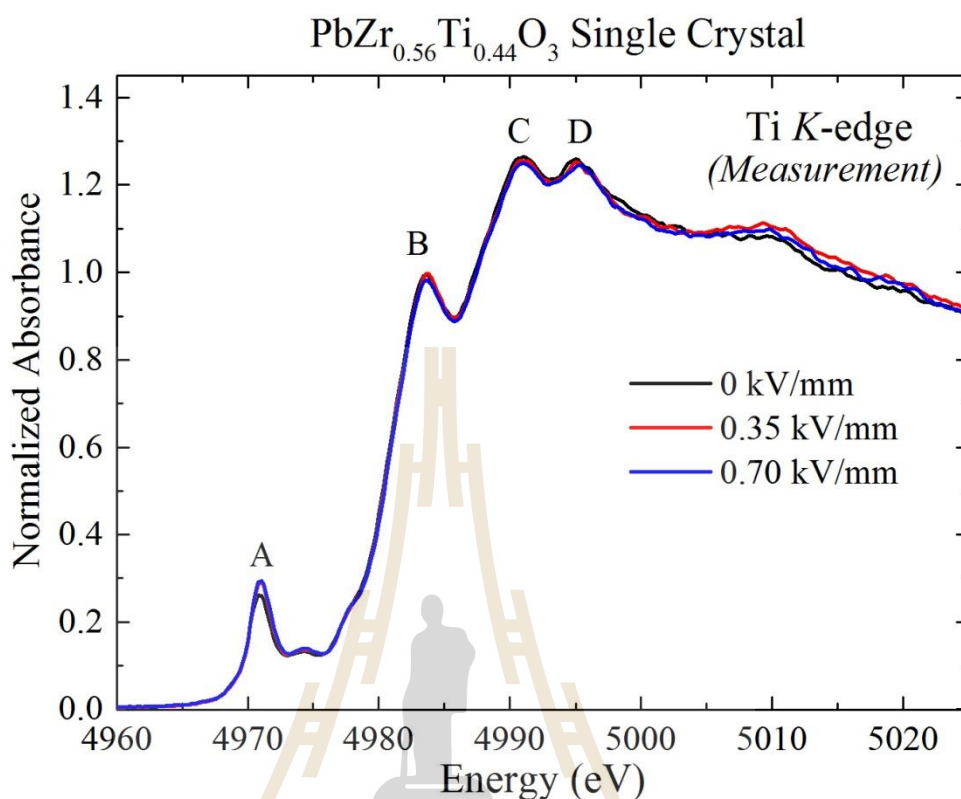
**Figure 4.7** Normalized Ti *K*-edge XANES spectra of PZT single crystal with x = 0.44 when applying electric field at 0 kV/mm, 0.35 kV/mm and 0.7 kV/mm.

Figure 4.7 shows the Ti K-edge XANES spectra of PZT with x = 0.44. The applied electric field was varied from 0 kV/mm, 0.35 kV/mm and 0.7 kV/mm. The integrated intensity of peak A is related to Ti displacement from center, while the integral intensity of peak B is a probability of electron 1s excite to 4p level or conduction band, and after peak is the back scattering of spherical wave electron with neighboring atoms.
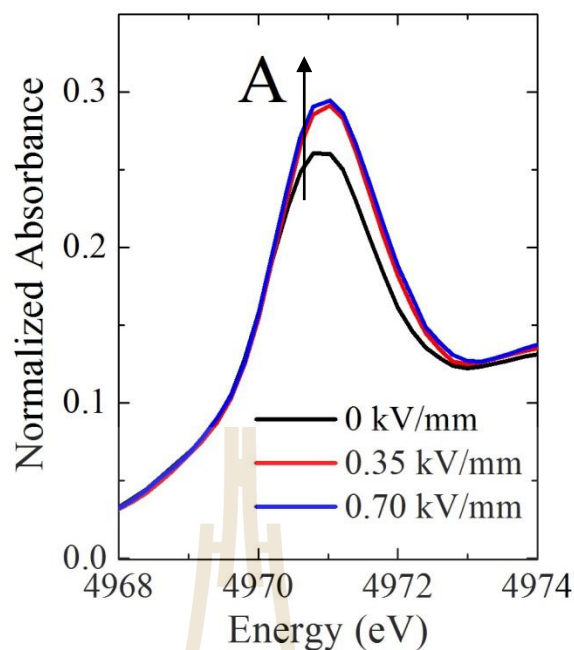
Figure 4.8 Normalized of XANE spectra of PZT with x=0.44 in the energy 4,968 eV to 4,974 eV when applied electric field at 0 kV/mm, 0.35 kV/mm and 0.7 kV/mm.

The integrated intensity of peak A relates to the Ti displacement off center of perovskite structure. When applying electric field, the integrated intensity of peak A increases, indicating that Ti atom moves off the center or polarization increases, as seen in the Figure 4.8. On the other hand, when electric field decreases, the integrated intensity of peak A decreases.

The displcement of Ti atom move from the center can be calculated by Vedrinskii method.The area under pre-edge is given by the equation $A = (\gamma_s/3)d_s^2$ where A is a peak area, d_s is the mean-squar displacement of The Ti atom from center and γ_s is an experimental determination of the constant in values of 12.5 eV/ Å^2 for PbTiO$_3$. To investigate the Ti-atom displacement, the calculation of area under peak A is listed in Table 4.1, showing The Ti- displacement as a function of the applied electric fields (as also plotted in Figure 4.9).

Table 4.1   The result of calculated area under pre-edge peak.

Applied Electric field	Area under the peak (eV (a.u.))	d_s (Å)
0 kV/mm	0.199	0.073
0.35 kV/mm	0.233	0.079
0.7 kV/mm	0.255	0.083
0.35 kV/mm return	0.245	0.081
0 kV/mm return	0.226	0.078
-0.35 kV/mm	0.226	0.078
-0.7 kV/mm	0.240	0.080
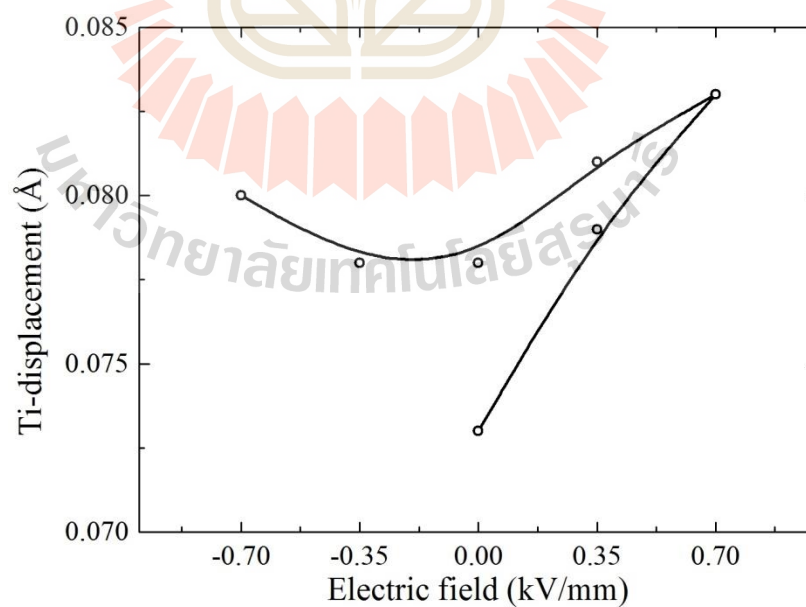
Figure 4.9   The Ti- displacement as a function of the applied electric fields.
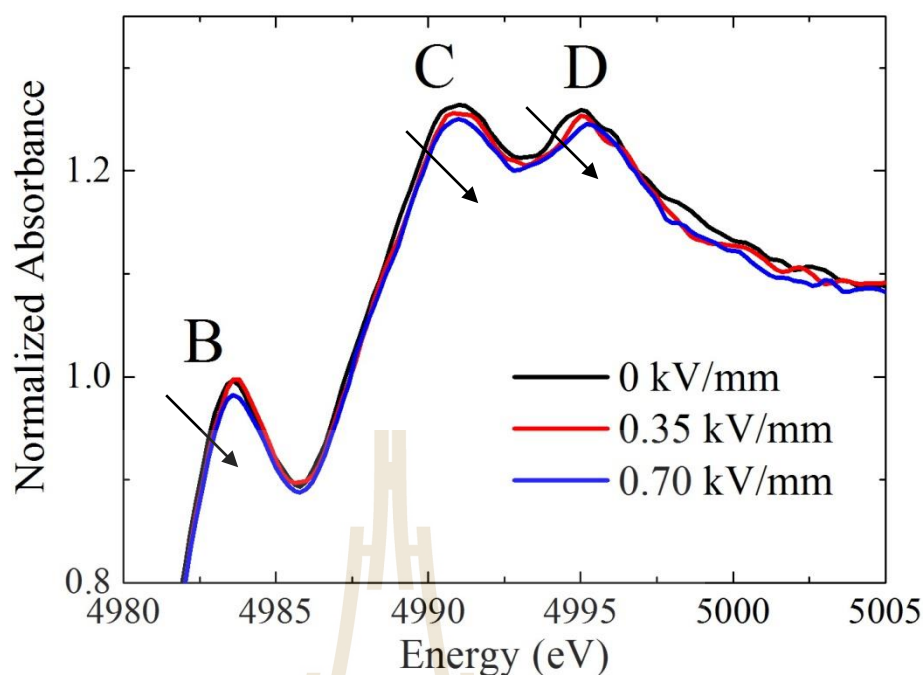
Figure 4.10 Normalized XANES spectra of PZT with x = 0.44 in the energy 4,985 eV to 5,005 eV when applied electric field at 0 kV/mm, 0.35 kV/mm and 0.07 kV/mm.

The intensity of peak B is a probability of electron 1s excite to 4p or conduction bands. As shown in Figure 4.10, the intensity of peak B, C and D increases with electric field. However, the intensity of peak C and D shows only very little change with the applied electric field.

The features of XANES spectrum is similar to the previous results by W. Kempet et al. (2013) result which included 4 peak intensities of XANES structure. However, both results have similar trends of intensities with opposite directions when applying electric field.
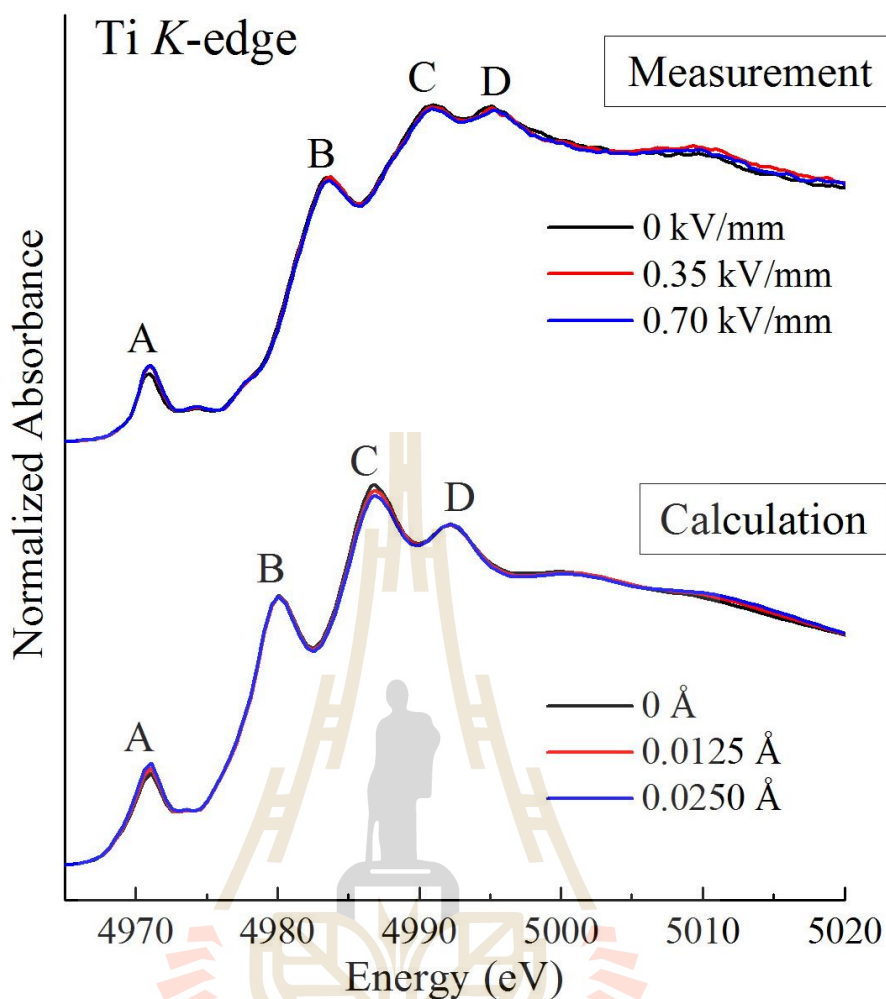
Figure 4.11 Ti K-edge XANE spectra of PZT with x = 0.44 single crystal at 0 kV/mm, 0.35 kV/mm and 0.07 kV/mm and calculated Ti K-edge XANES spectra at 0 Å, 0.0125 Å and 0.0250 Å of Ti off-center displacements by using FEFF8.2 program.

To support the experimental results, the Ti K-edge XANES spectra of PZT with tetragonal phase was calculated by using FEFF 8.2 program. The calculated XANE spectra under different Ti off-center positions which are in the range of 0 Å, 0.0125 Å and 0.0250 Å are shown in Figure 4.11. The experimental results show that the intensity of peak A increases and the intensity of peak B, C and D decreases with the amplitude of the field. The intensity of peak A, as shown in Figure 4.12(a), can be

compared very well with the calculation results in Figure 4.12(b). The intensity of peak B, C and D in the Figure 4.13(a) can also compare well with the calculation results, as shown in Figure 4.13(b), respectively. The changing intensity of peak A could be attributed to the small displacement of Ti atoms, indicating that the Ti atom off-center displacement is caused by the applied field. The calculated spectra related the change of all intensity due to small displacement (0 Å, 0.0125 Å and 0.0250 Å) of Ti atoms. The calculated intensity drops when the Ti atoms shift to a negative position. This simulation results are overall in good agreement with the experimental results.
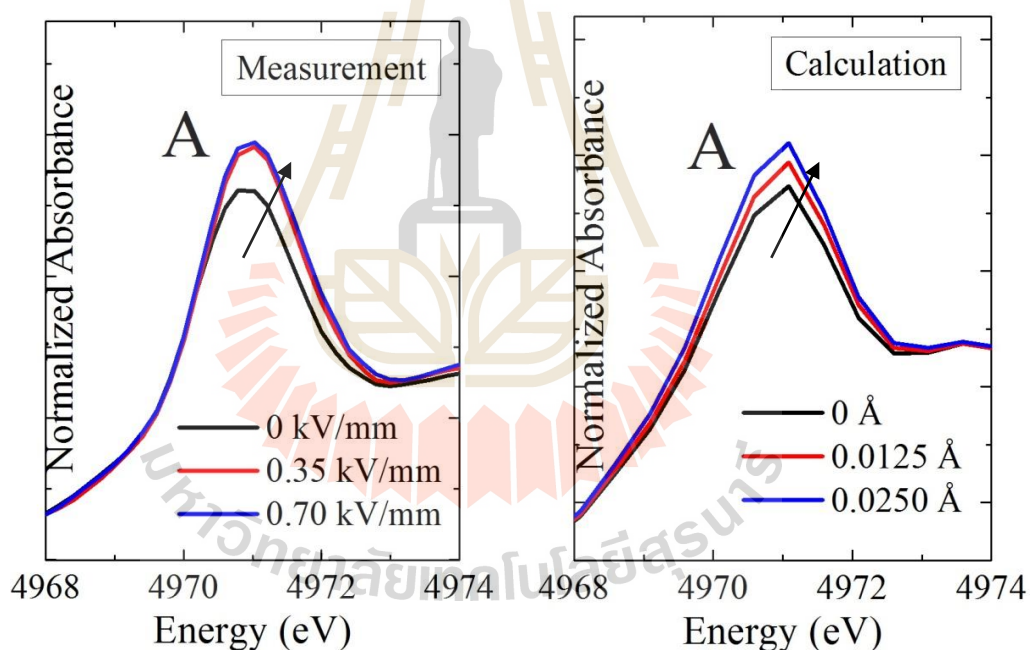
Figure 4.12 Ti K-edge XANE spectra of PZT with single crystal x = 0.44 zoom in the intensity of peak A. (a) compare with calculated spectrum (b) photon energy at 4,968-4,974 eV.
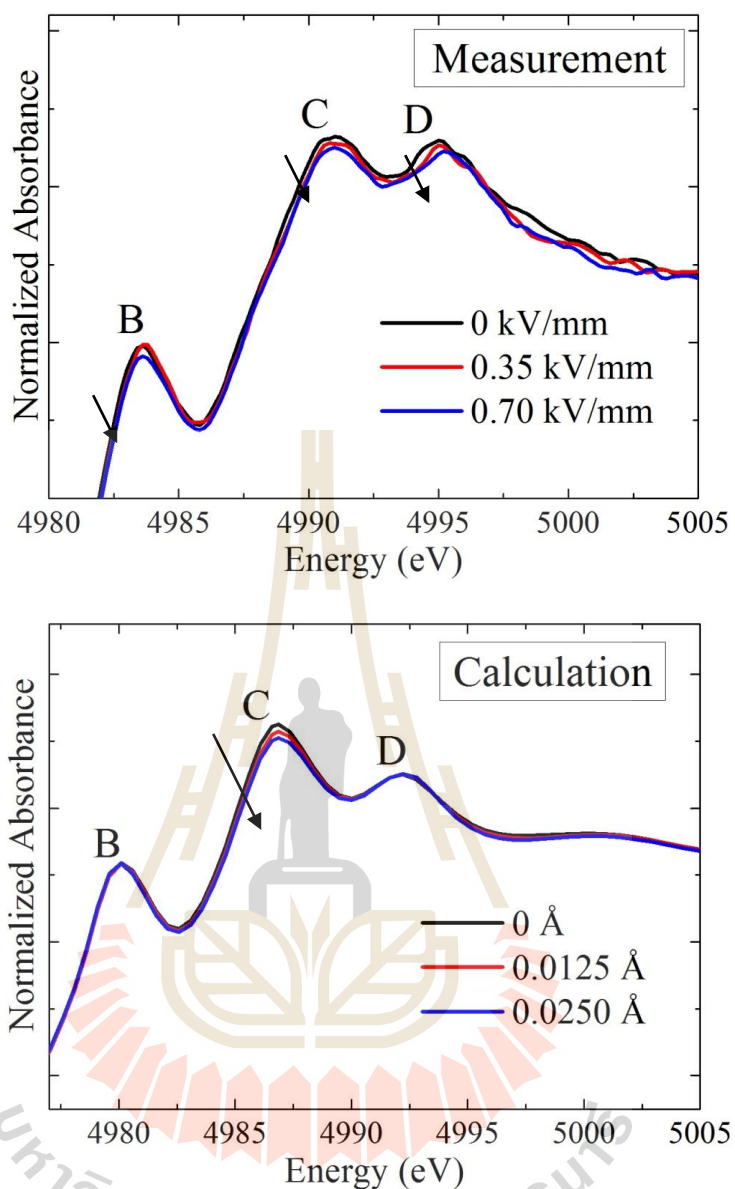
Figure 4.13 Ti K-edge XANE spectra of PZT single crystal with x = 0.44 zoom in the intensity of peak B, C and D (a) compare with calculated spectrum(b) photon energy at 4,980-5,005 eV.

The XANES calculation of PZT tetragonal structure completed with 4 main peak intensities. The results can be compared with previous work by W. Kempet et al.

(2013). Both results have the same intensity trend and feature. However, this calculation shows better agreement with the measurements.

4.3   Scanning electron microscope results

SEM is a type of electron microscope that produces images of a sample by scanning it with a focused beam of electrons. The electrons interact with atoms in the sample, producing various signals that can be detected and that contain information about the sample's surface topography and composition. Surface SEM analysis of PZT single crystal, shown in Figure 4.14(b), indicates the morphology in micrometer range without grain boundary, an observed for a typical characteristic of a single crystal.

(a)   (b)

Figure 4.14 (a) SEM analysis surface of PZT single crystal (x=0.44) in range 500 μm. (b) SEM analysis surface of PZT single crystal in range 1 μm.

4.4   Single crystal X-ray diffraction result

Crystal structure for PZT (x = 0.42) for the crystal system is reportedly triclinic, with unit cell dimensions a = 2.048Å, b = 3.052Å, c = 3.445Å and the angles α = 97.837°, β = 92.517°, γ = 89.461°. Crystal structure for PZT (x = 0.44) for the crystal system is monoclinic with unit cell dimensions a = 95.90 Å, b = 1.876 Å, c = 44.34 Å the angles α = 90°, β = 95.67°, γ = 90°. The present results are not reliable because the crystals are too small and there are too few spots of XRD pattern, as seen in Figure 4.16.
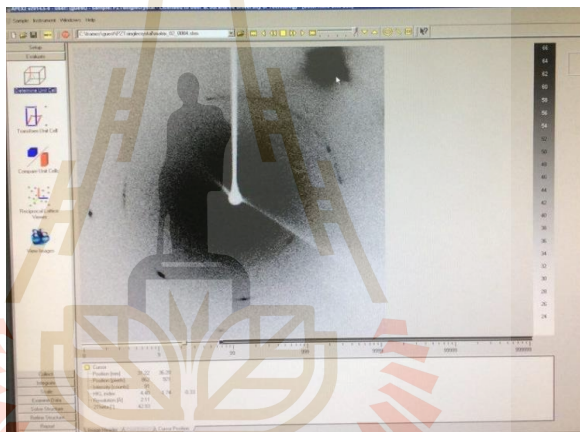
Figure 4.15 The spot of XRD pattern for PZT single crystal (x = 0.44) with XRD harvest spot program.

4.5   Atomic force microscopy results

PZT single crystal with x = 0.42 were heated at 100°C, 200°C, 300°C, 400°C and return at room temperature again. The results compose of three signals: the image of topography, EFM phase and EFM amplitude. The image gives three dimensions and the colors indictated the different depths in *nm* scale. The images of EFM phase show the area of different colors indicated that spontaneous polarization at room temperature

and 100°C when the spontaneous polarization decreases and vaguely at 200°C and 300°C, respectively. The AFM image at 400°C shows no spontaneous polarization. However, those reappear at room temperature again. The results comparing with the image of EFM phase are shown in Figure 4.16.
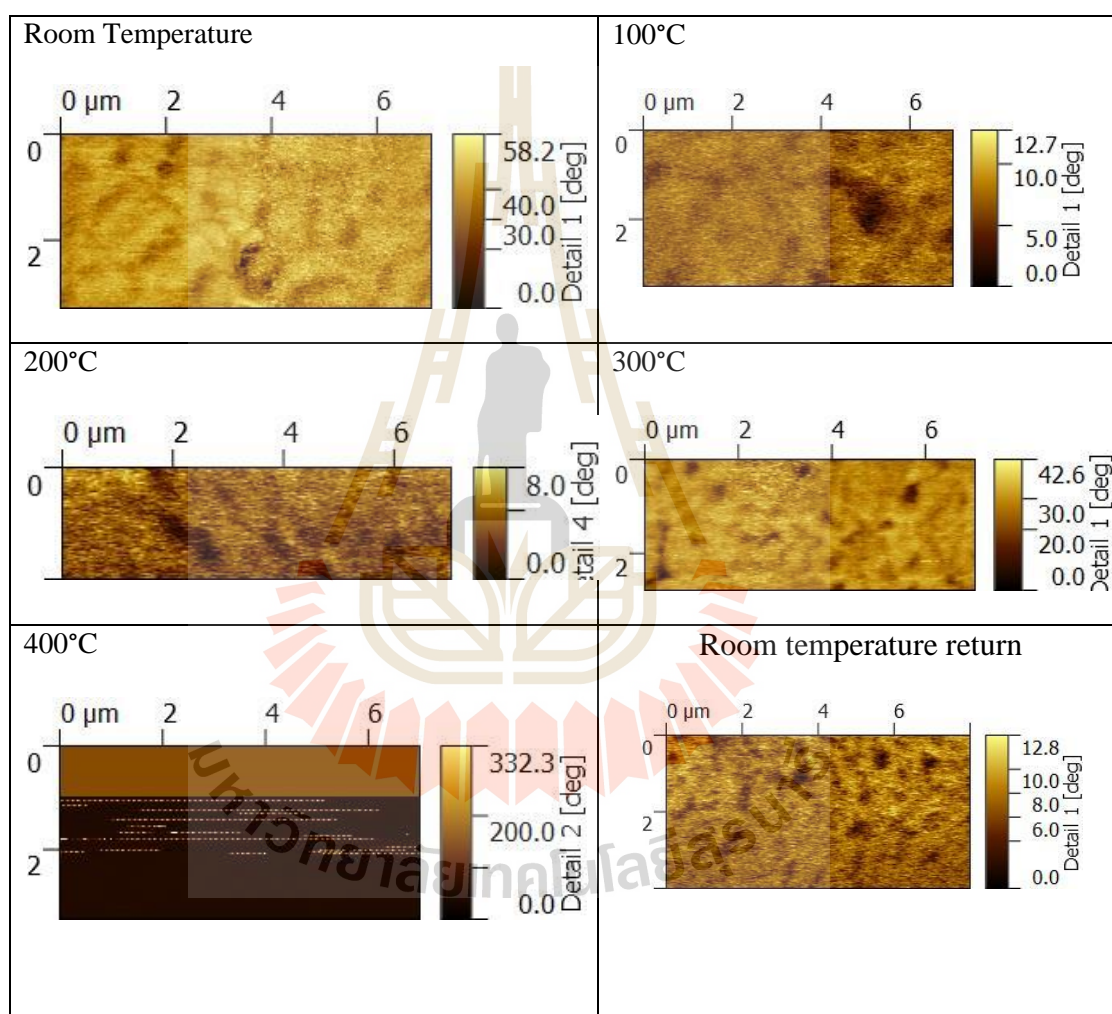
Figure 4.16 The result compare with the image of EFM phase.

CHAPTER V

CONCLUSIONS

This thesis studied the effects of temperature and electric field on local structure of PZT single crystals prepared by a top-seed melt growth method from Ye's group at Simon Fraser University. SEM results indicated the morphology in micrometer range without grain boundary observed, a typical characteristic of a single crystal. The results of AFM showed the spontaneous polarization decreased vaguely at 200°C-400°C and reappeared when returning the room temperature.

The XAS results of the shifted energy in the peak A as temperature increased while the intensities of peak B, C and D dropped in high temperature indicated that PZT tetragonal phase gradually changed, especially the decreasing of the c axis length, to cubic phase when the temperature increased.

For the electric field effect, the results showed that the changes of peak intensity were detected when applying the electric field. The change of the peak A intensity was the most sensitive to the amplitude of the applied field, while peak B, C and D the intensity was less sensitive to the field amplitude. The integrated intensity of peak A related to the Ti off center displacement in the perovskite structure. With applied electric field, the integrated intensity of peak A increased, indicating that Ti atom moved off the center or polarization increased.
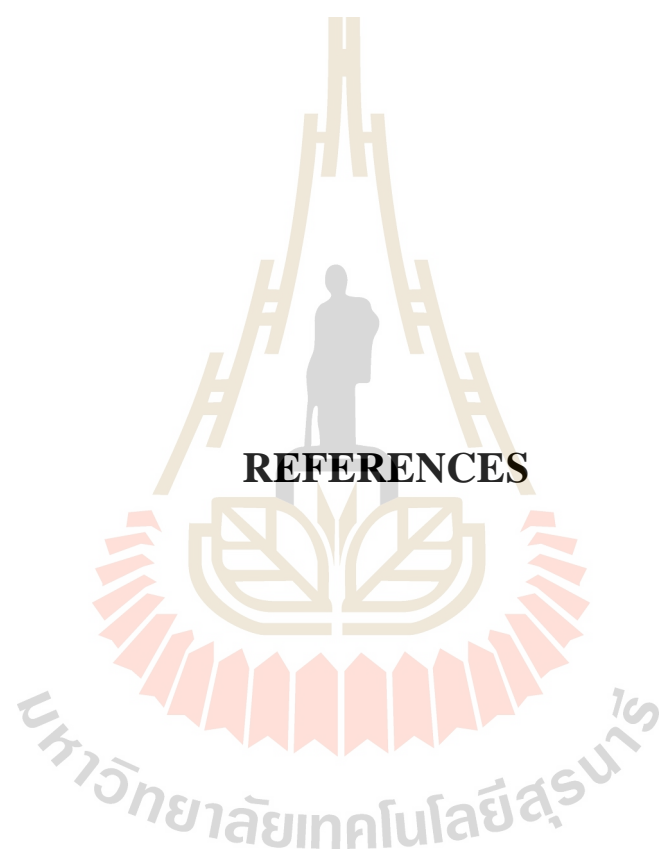
REFERENCES

REFERENCES

Ankudinov, A. L., Ravel, B., Rehr, J. J., and Conradsan, S. D. (1998). Real-space multiple-scattering calculation and interpretation of X-ray-absorption near-edge structure. **Phys. Rev.B.** 58: 7565.

Binnig, G., Quate, C. F., and Gerber, Ch. (1986). Atomic-force microscope. **Phys. Rev. Lett.** 56: 930-933.

Bellaiche, L., Garcia, A., and Vanderbilt, D. (2001). Electric-field induced polarization paths in $Pb(Zr_{1-x}Ti_x)O_3$ alloys. **Phys. Rev.B.** 6406: 060103-1-060103-4.

Cao, D., Jeong, I. K., Heffner, R. H., Darling, T., and Lee, J. K. (2004). Local structure study of the off center displacement of Ti and Zr across the morphotropic phase boundary of $PbZr_{1-x}Ti_xO_3$, x=0.40, 0.47, 0.49, 0.55. **Phys. Rev. B.** 70: 224102-1-224102-7.

Cappella, B., and Dietler, G. (1999). Force-distance curves by atomic force microscopy Surface Science Reports. 34

Cook, W. R., Jae, B., and Jae, H. (1971). **Piezoelectric ceramics. Academic Press London**, vol.1.

Frantti, J., Eriksson, S., Hull, S., Kakihana, M., Lantto, V., and Rundlo, H. (2003). Composition variation and the monoclinic phase within $Pb(Zr_xTi_{1-x})O_3$ ceramics. **J. Phys. Condensed Matter** 15.

Geisse, Nicholas A. (2009). AFM and combined optical techniques. **Materials Today.** 12: 40-45.

Giessibl, Franz J. (2003). Advances in atomic-force microscopy. **Material of Modern Physics.** 75(3): 949-983.

Griffith, J. S., and Orgel, L. E. (1957). Ligand-field theory. **Q. Rev. Chem. Soc.** 11: 381-393.

Gross, L., Mohn, F., Moll, N., Liljeroth, P., and Meyer, G. (2009). The Chemical structure of a molecule resolved by atomic force microscopy. **Science** 325 (5944): 1110-1114.

Hall, D. A., Steuwer, A., Cherdhirunkorn, B., Mori, T., and Withers, P. J. (2006). Identification of crystalline elastic anisotropy in PZT ceramics from in-situ blocking stress measurements. **Acta Mater.** 54: 3075.

Hooker, M. W. (1998). Properties of PZT based piezoelectric ceramic between 150°C and 250°C. **Lockheed Martin Engineering and Science Co**, Hampton, Virginia.

Jaff, B., Cook, W. R., and Jaffe, H. L. (1971). **Piezoelectric ceramics. London.** p 136.

Jiang W. B., Yang L., Guo, C. Y., Hu, Z., Lee, J. M., Smidman, M., Wang, Y. F., Shang T., Cheng, Z. W., Gao, F., Ishii, H., Tsuei, K. D., Liao, Y. F., Lu X., Tjeng, L. H., Chen, J. M., and Yuan, H. Q. (2015). Crossover from a heavy fermion to intermediate valence state in noncentrosymmetric $Yb_2Ni_{12}(P,As)_7$. **Scientific Reports** 5: 17608.

Jones, J. L., Hoffman, M., and Vogel, S. C. (2007). In situ neutron diffraction studies of a commercial, soft lead zirconate titanate ceramic: response to electric fields   and mechanical stress. **Mech Mater.** 39: 283.

Jutimoosik, J. (2010). Local Structure of Magnesium Zinc Oxide Nanocrystals. M.S. thesis, Suranaree University of Technology, Nakorn Ratchasima.

Jutimoosik, J., Hunpratub, S., Maensiri, S., Rujirawat, S., and Yimnirun, R. (2014). On preferred   Mn site in multiferroic $BiFeO_3$: A view by synchrotron X-ray absorption near edge structure spectroscopy. **J. App. Phys.** 116: 104105.

Kempet, W., Marungsri, B., Yimniran, R., Klysubun, W., and Pojprapai, S. (2013). Investigation of the unit cell distortion in PZT ceramic via in-situ XAS technique. **Ferroelectrics** 453: 1, 106-112.

Lines, M. E., and Glass, A. M. (2001). **Principles and applications of ferroelectrics and related materials**, Oxford University Press, USA.

Newville, M. (2004). **Fundamental of XAFS Consortium for Advanced Radiation Sources**, University of Chicago, Chicago.

Noheda B., Gonzalo, J. A., Cross, L. E., Guo R., Park, S. E., Cox, D. E., and Shirane, G. (2000). A tetragonal to monoclinic phase transition in a ferroelectric perovskite the structure of $PbZr_{0.52}Ti_{0.48}O_3$. **Phys. Rev. B.** 63.

Pojprapai (Imlao), S., Jones, L. J., Studer, J. A., Russell, J., Valanoor, N., and Hoffman, M. (2008). Dynamic processes of domain switching in lead zirconate titanate under cyclic mechanical loading by in situ neutron diffraction. **Acta Mater.** 58(6): 1897-1908.

Rehr, J. J., and Albers, R. C. (2000). Theoretical approaches to x-ray absorption fine structure. **Rev. Mod. Phys.** 72: 621.

Singh, A. K. (2008). Magnetic Perovskites: Synthesis, Structure and Physical Properties**. Phys Lett.** 92.

Vedrinskii, R. V., Kraizman, V. L., Novakovich, A. A., Demekhin, P. V., and Urazhdin, S. V. (1998). Pre-edge fine structure of the 3d atom K X-ray absorption spectra and quantitative atomic structure determinations for ferroelectric perovskite structure crystals. **J. Phys. Condensed Matt.** 10: 9561.

Vuong Le Dai, Gio Phan Dinh, Chuong Truong Van, Trang i Dung Thi Hoa, Hung Duong, and Viet Du Nguyen Trung. (2013). Effect of Zr/Ti ratio content on some physical properties of low temperature sintering PZT-PZN-PMnN Ceramics. **Inter. J. Mat. and Chem.** 3(2): 39-43.

Wang, C. H., Chang, S. J., and Chang, P. C. (2004). Effect of sintering conditions on characteristics of $PbTiO_3$-$PbZrO_3$-$Pb(Mg_{1/3}Nb_{2/3})O_3$-$Pb(Zn_{1/3}Nb_{2/3})O_3$. **Mat. Scie. Eng. B.** 111: 124-130.

Xie, Y. (2013). Synthesis and Characterization of Piezo-ferroelectric Lead Zirconate Titanate (PZT) Single Crystals and Related Ternary Ceramics, Simon Fraser University, Canada.

Yoon, S., and Baik, S. (2006). Formation mechanisms of tetragonal barium titanate nanoparticles in alkoxide–hydroxide sol-precipitation synthesis. **J. Amer. Ceram. Soc.** 89: 1816-1821.

Zhong, Q., Inniss, D., Kjoller, K., and Elings, V. (1993). Fractured polymer/silica fiber surface studied by tapping mode atomic-force microscopy. **Sur. Sci. Lett.** 290: 688.
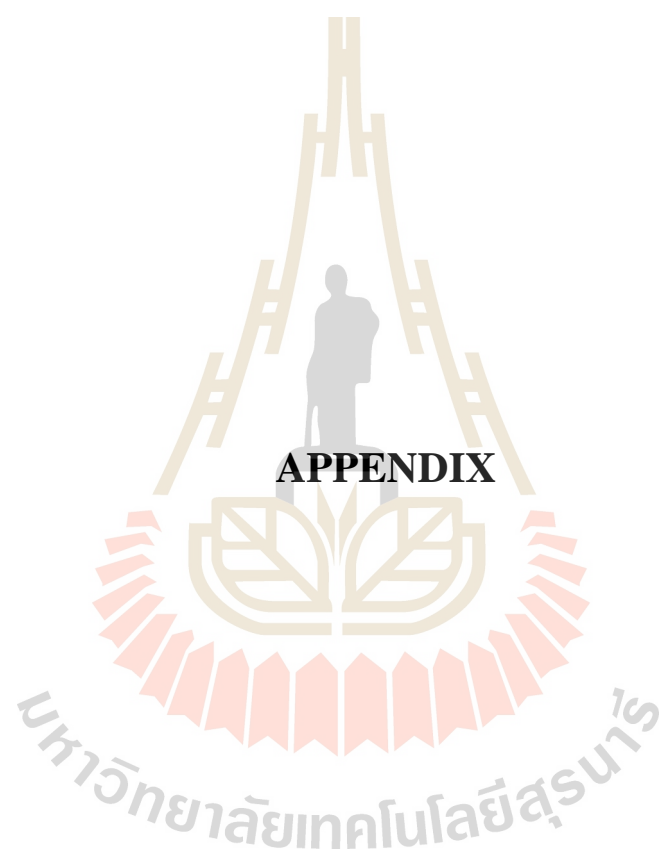
APPENDIX

APPENDIX

ATOM INPUT OF TETRAGONAL STRUCTURE FROM

FEFF PROGRAM

```
title PbTiO3  tetra structure
rmax=7
a=3.885 c=4.139
space P 4 m m
core=Ti
atom
Pb   0.00000        0.00000        0.00000
Ti   0.50000        0.50000        0.53770
O    0.50000        0.50000        0.11180
O    0.50000        0.00000        0.61740


* This feff.inp file generated by ATOMS, version 2.50
 * ATOMS written by and copyright (c) Bruce Ravel, 1992-1999

 * -- * -- * -- * -- * -- * -- * -- * -- * -- * -- * -- * -- * -- *
-- * -- *
 *       total mu =     5269.6 cm^-1, delta mu =      772.6
cm^-1
 *       specific gravity =  8.057, cluster contains  123
atoms.
 * -- * -- * -- * -- * -- * -- * -- * -- * -- * -- * -- * -- * -- *
-- * -- *
 *       mcmaster corrections:  0.00093 ang^2 and  0.165E-05
ang^4
 * -- * -- * -- * -- * -- * -- * -- * -- * -- * -- * -- * -- * -- *
-- * -- *

 TITLE   PbTiO3  tetra structure

 EDGE       K
 S02        1.0

 *        pot    xsph   fms   paths genfmt ff2chi
 CONTROL 1      1      1      1      1       1
 PRINT   1      0      0      0      0       0
    *       r_scf  [ l_scf  n_scf  ca ]
 SCF     4.0         15     30     0.1l
```

```
*           ixc  [ Vr   Vi ]
 EXCHANGE  0       0    0
*EXAFS
*RPATH     7.75632

*           kmax  [ delta_k  delta_e ]
XANES      5.5      0.07     0.5
*           r_fms      [ l_fms ]
FMS        7                  0
*
RPATH      0.10000
*           emin  emax  resolution
LDOS      -20     20   0.1

 POTENTIALS
 *   ipot   z [ label    l_scmt   l_fms   stoichiometry ]
       0   22    Ti       -1       -1          0
       1    8    O        -1       -1          3
       2   82    Pb       -1       -1          1
       3   22    Ti       -1       -1          0.44
       4   40    Zr       -1       -1          0.56

 ATOMS
   0.00000      0.00000      0.00000     0   Ti
0.00000
   0.00000      0.00000     -1.76280     1   O
1.76280
  -1.94250      0.00000      0.32988     1   O
1.97031
   1.94250      0.00000      0.32988     1   O
1.97031
   0.00000     -1.94250      0.32988     1   O
1.97031
   0.00000      1.94250      0.32988     1   O
1.97031
   0.00000      0.00000      2.37620     1   O
2.37620
  -1.94250     -1.94250      1.91346     2   Pb
3.34783
  -1.94250      1.94250      1.91346     2   Pb
3.34783
   1.94250      1.94250      1.91346     2   Pb
3.34783
   1.94250     -1.94250      1.91346     2   Pb
3.34783
  -1.94250      1.94250     -2.22554     2   Pb
3.53548
  -1.94250     -1.94250     -2.22554     2   Pb
3.53548
   1.94250      1.94250     -2.22554     2   Pb
3.53548
   1.94250     -1.94250     -2.22554     2   Pb
3.53548
```

```
   0.00000      3.88500      0.00000    3   Ti
3.88500
  -3.88500      0.00000      0.00000    3   Ti
3.88500
   0.00000     -3.88500      0.00000    3   Ti
3.88500
   3.88500      0.00000      0.00000    4   Zr
3.88500
   0.00000      0.00000     -4.13900    4   Zr
4.13900
   0.00000      0.00000      4.13900    4   Zr
4.13900
   0.00000      3.88500     -1.76280    1   O
4.26623
   0.00000     -3.88500     -1.76280    1   O
4.26623
   3.88500      0.00000     -1.76280    1   O
4.26623
  -3.88500      0.00000     -1.76280    1   O
4.26623
   1.94250      0.00000     -3.80912    1   O
4.27583
  -1.94250      0.00000     -3.80912    1   O
4.27583
   0.00000     -1.94250     -3.80912    1   O
4.27583
   0.00000      1.94250     -3.80912    1   O
4.27583
   1.94250     -3.88500      0.32988    1   O
4.35607
   1.94250      3.88500      0.32988    1   O
4.35607
   3.88500     -1.94250      0.32988    1   O
4.35607
  -3.88500      1.94250      0.32988    1   O
4.35607
   3.88500      1.94250      0.32988    1   O
4.35607
  -1.94250     -3.88500      0.32988    1   O
4.35607
  -1.94250      3.88500      0.32988    1   O
4.35607
  -3.88500     -1.94250      0.32988    1   O
4.35607
   0.00000     -3.88500      2.37620    1   O
4.55407
   0.00000      3.88500      2.37620    1   O
4.55407
  -3.88500      0.00000      2.37620    1   O
4.55407
   3.88500      0.00000      2.37620    1   O
4.55407
```

```
   1.94250      0.00000      4.46888    1    O
4.87280
   0.00000     -1.94250      4.46888    1    O
4.87280
   0.00000      1.94250      4.46888    1    O
4.87280
  -1.94250      0.00000      4.46888    1    O
4.87280
   3.88500     -3.88500      0.00000    3    Ti
5.49422
  -3.88500      3.88500      0.00000    3    Ti
5.49422
  -3.88500     -3.88500      0.00000    3    Ti
5.49422
   3.88500      3.88500      0.00000    3    Ti
5.49422
   3.88500      0.00000     -4.13900    3    Ti
5.67667
  -3.88500      0.00000      4.13900    3    Ti
5.67667
   0.00000      3.88500     -4.13900    3    Ti
5.67667
   0.00000     -3.88500      4.13900    3    Ti
5.67667
   0.00000     -3.88500     -4.13900    3    Ti
5.67667
  -3.88500      0.00000     -4.13900    3    Ti
5.67667
   0.00000      3.88500      4.13900    3    Ti
5.67667
   3.88500      0.00000      4.13900    3    Ti
5.67667
  -3.88500      3.88500     -1.76280    1    O
5.77009
   3.88500     -3.88500     -1.76280    1    O
5.77009
  -3.88500     -3.88500     -1.76280    1    O
5.77009
   3.88500      3.88500     -1.76280    1    O
5.77009
   3.88500      1.94250     -3.80912    1    O
5.77719
  -1.94250      3.88500     -3.80912    1    O
5.77719
  -3.88500     -1.94250     -3.80912    1    O
5.77719
   3.88500     -1.94250     -3.80912    1    O
5.77719
  -1.94250     -3.88500     -3.80912    1    O
5.77719
   1.94250     -3.88500     -3.80912    1    O
5.77719
```

-3.88500	1.94250	-3.80912	1	O
5.77719				
1.94250	3.88500	-3.80912	1	O
5.77719				
-5.82750	0.00000	0.32988	1	O
5.83683				
0.00000	5.82750	0.32988	1	O
5.83683				
0.00000	-5.82750	0.32988	1	O
5.83683				
5.82750	0.00000	0.32988	1	O
5.83683				
0.00000	0.00000	-5.90180	1	O
5.90180				
3.88500	-3.88500	2.37620	1	O
5.98605				
-3.88500	-3.88500	2.37620	1	O
5.98605				
3.88500	3.88500	2.37620	1	O
5.98605				
-3.88500	3.88500	2.37620	1	O
5.98605				
3.88500	1.94250	4.46888	1	O
6.23197				
-3.88500	1.94250	4.46888	1	O
6.23197				
3.88500	-1.94250	4.46888	1	O
6.23197				
1.94250	-3.88500	4.46888	1	O
6.23197				
-1.94250	-3.88500	4.46888	1	O
6.23197				
-1.94250	3.88500	4.46888	1	O
6.23197				
-3.88500	-1.94250	4.46888	1	O
6.23197				
1.94250	3.88500	4.46888	1	O
6.23197				
5.82750	-1.94250	1.91346	2	Pb
6.43385				
1.94250	5.82750	1.91346	2	Pb
6.43385				
-5.82750	1.94250	1.91346	2	Pb
6.43385				
1.94250	-5.82750	1.91346	2	Pb
6.43385				
-1.94250	5.82750	1.91346	2	Pb
6.43385				
-1.94250	-5.82750	1.91346	2	Pb
6.43385				
-5.82750	-1.94250	1.91346	2	Pb
6.43385				

5.82750	1.94250	1.91346	2	Pb
6.43385				
0.00000	0.00000	6.51520	1	O
6.51520				
5.82750	1.94250	-2.22554	2	Pb
6.53346				
5.82750	-1.94250	-2.22554	2	Pb
6.53346				
1.94250	5.82750	-2.22554	2	Pb
6.53346				
-5.82750	1.94250	-2.22554	2	Pb
6.53346				
1.94250	-5.82750	-2.22554	2	Pb
6.53346				
-1.94250	5.82750	-2.22554	2	Pb
6.53346				
-5.82750	-1.94250	-2.22554	2	Pb
6.53346				
-1.94250	-5.82750	-2.22554	2	Pb
6.53346				
-1.94250	-1.94250	6.05246	2	Pb
6.64672				
1.94250	-1.94250	6.05246	2	Pb
6.64672				
-1.94250	1.94250	6.05246	2	Pb
6.64672				
1.94250	1.94250	6.05246	2	Pb
6.64672				
3.88500	3.88500	-4.13900	3	Ti
6.87879				
-3.88500	3.88500	4.13900	3	Ti
6.87879				
3.88500	-3.88500	4.13900	3	Ti
6.87879				
3.88500	-3.88500	-4.13900	3	Ti
6.87879				
-3.88500	3.88500	-4.13900	3	Ti
6.87879				
-3.88500	-3.88500	4.13900	3	Ti
6.87879				
-3.88500	-3.88500	-4.13900	3	Ti
6.87879				
3.88500	3.88500	4.13900	3	Ti
6.87879				
1.94250	1.94250	-6.36454	2	Pb
6.93210				
1.94250	-1.94250	-6.36454	2	Pb
6.93210				
-1.94250	-1.94250	-6.36454	2	Pb
6.93210				
-1.94250	1.94250	-6.36454	2	Pb
6.93210				

```
   0.00000     -5.82750     -3.80912     1   O
6.96198
   0.00000      5.82750     -3.80912     1   O
6.96198
  -5.82750      0.00000     -3.80912     1   O
6.96198
   5.82750      0.00000     -3.80912     1   O
6.96198
 END
```

CURRICULUM VITAE

Name   Rojnapa Tharamas

Date of Birth 25 December 1990

Place of Birth Yasothon, Thailand

Education

7 June 2012   Mahasarakham University,Mahasarakham,Thailand Bachelor of Science

(Physics)

Academic Experience

1. Research Assistant at Synchrotron Light Research Institute (Public Organization),

Thailand.

2. Teaching Assistant at Laboratory, School of Physics, Suranaree University of

Technology, Thailand.